Synthesis of nanostructured rare earth metal doped Sr_2TiFeO_6 (STF) double perovskites electrocatalysts for water splitting reactions

By

Muhammad Zeeshan

School of Chemical and Material Engineering

National University of Sciences and Technology

2022

Synthesis of nanostructured rare earth metal doped Sr$_2$TiFeO$_6$ (STF) double perovskites electrocatalysts for water splitting reactions

Name: Muhammad Zeeshan

Registration No: 00000319417

This thesis is submitted as partial fulfillment of the requirements for the degree of

"MS in Chemical Engineering"

Supervisor Name: Dr. Erum Pervaiz

School of Chemical and Material Engineering (SCME)

National University of Sciences & Technology (NUST)

H-12 Islamabad, Pakistan

April, 2022

Dedication

By the grace of Almighty Allah, who is the most Beneficent and the most merciful.

This research is dedicated to my parents, who have always been my source of guidance and support.

To my supervisor who shared her knowledge, gave advice and encouraged me to fulfill my tasks.

And to all my fellows, with whom I worked with and shared good memories.

Acknowledgement

There is no one except Almighty Allah, whose will is necessary for everything and anything in this world, who favored us with the capacity to think and made us anxious to investigate this entire universe. Infinite greetings upon the Holy Prophet Muhammad (PBUH), the reason for the creation of the universe and wellspring of information and blessing for whole humankind.

Abstract

The electrochemical water splitting is well-thought-out as a clean source to produce water splitting and for the use of different energy applications. But there is a still problem is present to produce the hydrogen on the large scale, the problem is mainly concern with the stability and efficiency of the electrocatalysts and also in Hydrogen Evolution Reaction in acidic media as well as different kinetics and values of high overpotential of four-electron transfer Oxygen Evolution Reaction OER. Thus, this research based on electrocatalysts that helps to reduce the overpotential for the OER/HER. The synthesis of double perovskites electrocatalysts for high stability and the effective activity towards electrolysis of water was important for the production of hydrogen. In this study, pure (Sr_2TiFO_6) STF based double perovskites and STF/Pr doped electrocatalysts by doping the rare earth metal praseodymium Pr at A-site and B-site were made by sol-gel method. The Sr_2TiFO_6 (STF) based electrocatalysts was characterized by XRD, SEM and FTIR and electrochemical performance was analyzed by using 3-electrode testing in alkaline media. The results of STF Sr_2TiFO_6 (STF) based double perovskites towards OER (Oxygen Evolution Reaction) and HER (Hydrogen Evolution Reaction) was very remarkable. The OER results showed overpotential of 230 at current density of 10mA/cm^2 and Tafel slope was 139 mV dec^{-1}. For HER, there was overpotential of 194mV at current density of 10mA/cm^2 and Tafel slope was 126 mV dec^{-1}. Moreover, it exhibits notable results of durability for 24 hours. With the help of Sr_2TiFO_6 (STF) based double perovskites electrocatalysts, we can develop more efficient process and enhance the activity towards water splitting reactions.

Key Words:

Water splitting, Oxygen evolution reaction (OER), Perovskites, Double Perovskite, Hydrogen evolution reaction (HER)

Table of Contents

List of Figures

List of Tables

Abbreviations

Oxygen evolution reaction   OER

Hydrogen evolution reaction   HER

Sr_2TiFeO_6 STF

Nickle   Ni

Strontium: Sr

Praseodymium: Pr

Titanium: Ti

Oxidation: Ox

Reduction: Red

Iron   Fe

Oxygen   O

Layered double hydroxide   LDH

2 Dimensional   2D

ECSA:Electrochemically active surface area   ECSA

Platinum   Pt

Chapter 1

Introduction

An energy system which is sustainable as well as eco-friendly and with least consumption of natural sources is one of the pivotal targets of scientist for future [3, 4]. Since 2013, global energy consumption has risen to 18 TW, with natural energy supplies such as gas, oil, and coal providing 80% of the supply [5]. Up to 2040, the growth in global energy consumption is expected to be 24 or 26 TW, depending on whether "new policies" or "existing policies" are used. Also, the increase in carbon dioxide emissions is predicted to be 37 or 44 Gt yr-1 in 2040, which was recorded to be 32 Gt yr-1 in 2013. And all this is to happen because of the rapid population growth and increased industrialization. The situation seems quite alarming because of the increase in energy demand and supply and a drastic decrease in the sources responsible for its production. Given to this, the world is putting its thought and resources to develop energy systems which consume renewable energy sources (wind energy, solar power and hydroelectric power) for the sake of preservation of nature and climate [6].

An increase in the production and usage of renewable resources in electricity sector is pivotal, from the figures of 2010 it was only 2.1 TW out of 17.6 TW which is 12 % of the global energy demand. The increased penetration of renewable resources is also required in transportation and chemical industry which was 19 % in 2010, i.e., 3.3 TW out of 17.6 TW, where 43% (1.4TW) of it was by light duty vehicles and the rest 57 % (1.9 TW) was consumed by heavy duty vehicles, rail, aviation and marine. Among the consumption by light duty vehicles electrification (electric cars) is already decarbonizing the environment but electrification in heavy duty vehicles is quite difficult. As a result, it is anticipated that among light duty vehicles the energy demand will remain the same or even decrease but the consumption of energy by commercial transportation will rise by approximately 2/3 from 2010 to 2040, which is 1.9 to 3.2 TW. In the same way the energy demand in chemical industry is currently 8 % of global energy which is (1.5 TW) which is likely to grow by 2/3 from 2010 to 2040 which is 1.5 TW to 2.5 TW as the worldwide demand of plastic and fertilizer will increase [7]. Owing to all these circumstances the world is focusing on the production of chemical fuels which are sustainable and are a much more natural and cheap resource of energy. For this the industrial chemicals like, ammonia (175 Mt yr-1),

hydrogen peroxide (2.2 Mt yr-1), hydrogen (50 Mt yr-1), propylene (73 Mt yr-1), ethylene (115 Mt yr-1), methanol (40 Mt yr-1) etc., could be used as a sustainable energy resource for the production of chemicals to make products needed worldwide on daily basis with reduced emission of CO2 [8]. **Fig 1**
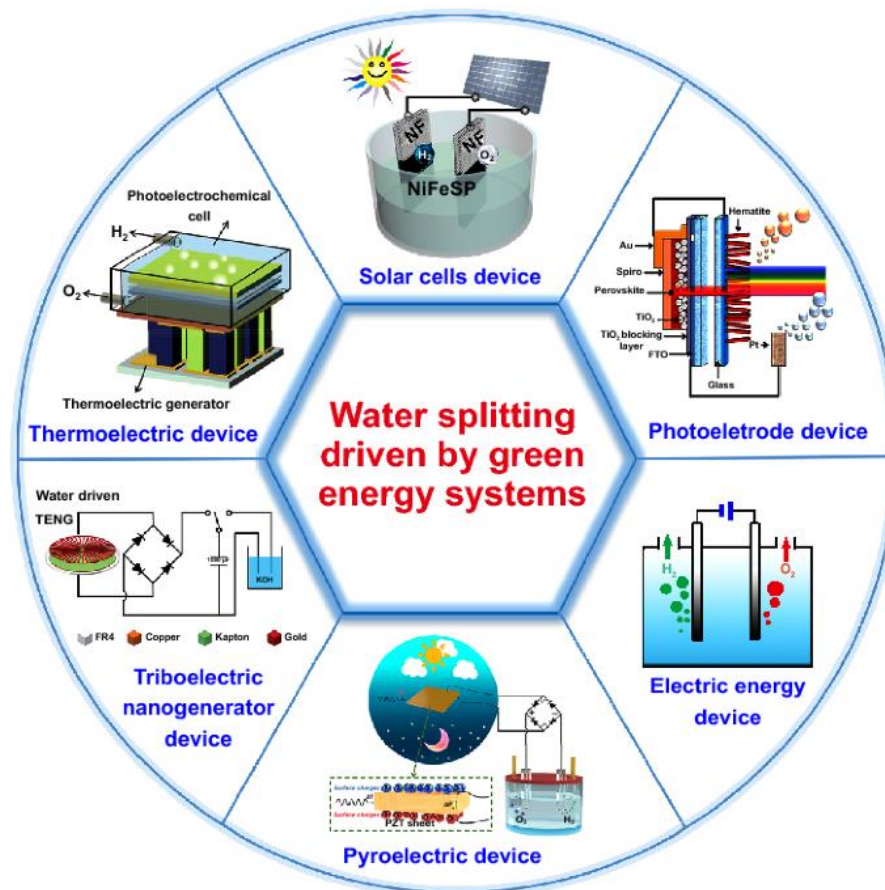
Figure 1: Schematic diagram of different resources of water splitting [1]

The Earth's atmosphere contains CO2, nitrogen and water which can be used for the production of hydrocarbons, ammonia and oxygenates. These can then be utilised to make critical fuels and chemicals using renewable energy electrochemical processes, but only if catalysts with the right characteristics can be produced. For instance, for a sustainable source of hydrogen, water splitting reaction (Half-reactions of hydrogen and oxygen evolution) is of great scope [9, 10]. The stable hydrogen produced is used in a number of applications, including fuel cells, which convert chemical energy to electrical energy by oxidising hydrogen and reducing oxygen, and hydrogen peroxide, which is used in the water treatment industry and in pulp/paper bleaching. In the same way, CO2 in the atmosphere or coming from other sources can be used for the production of certain fuels, chemicals, polymers and plastics by preliminary

electroreduction [5]. Similarly, nitrogen going through electrochemical process produces ammonia which is used for fertilizer production, and also on their application in a required concentration, also in Haber Bosch process and in the prevention of environmental hazards in case of run off. Given to all these uses of these natural resources an efficient and improved electrocatalysts with selective abilities for specific transformations is crucial [6].

For an enhanced electrocatalytic system two main methods are used

i. By providing more active sites on given electrode.
ii. Increasing each active site's intrinsic activity.

The respective ways are mutually exclusive and in an ideal case can be addressed simultaneously, thus giving the utmost improvement. But there are limitations to them as well such as, the maximum amount of charge that can be loaded on the electrode leaving the processes such as charge and mass transport unaffected.

Electrochemical water splitting is an excellent technique for producing oxygen and hydrogen [11, 12]. However, the deciding stage of the water-splitting process, the oxygen evolution reaction (OER), that necessitates the four proton-coupled electron transfers as well as the creation of an oxygen-oxygen bond, is a sluggish and dallying process that necessitates the use of a catalyst [13-15]. Oxides or inert metals, such as IrO_2 and RuO_2 and, have long been regarded "state of the art" electrocatalysts for the oxygen evolution process, but due to expensive and scarcity have hampered their widespread use [16, 17]. Furthermore, they can oxidise in alkaline electrolytes because they are unstable metals, As a result of these factors, considerable study and research is underway to investigate alternatives with advantages such as cheap cost, earth abundance, high efficiency, and stability [18, 19].

Hydrogen production on a huge scale from water splitting techniques, significant effort is necessary to create catalytically active and cost-effective electrocatalysts. Many inexpensive earth-abundant materials, such as metals phosphides, carbides [20], transition metal oxides[21] (for example, spinel oxides and perovskites), layered double hydroxides and carbonaceous materials [22, 23], transition metal dichalcogenides [24] [25], and selenides have been studied extensively for OER over the past few year [26, 27]. However, using most common metal catalysts are still problematic for HER, since a catalyst with increased OER activity may not be active

for HER. As a result, a bifunctional electrolysis cell fails to fulfil the electrocatalytic performance criteria for the total water splitting process. As a result of these difficulties, scientists must design a robust bifunctional electrocatalyst that is equally active in both the OER and HER reactions.

Now a days, whole world suffering energy rises and also different environmental issues. World scientist has been struggling to find a renewable energy resources that can be replaced with fossil fuels. Hydrogen production on a huge scale from water splitting techniques, significant effort is necessary to create catalytically active and cost-effective electrocatalysts. Many inexpensive earth-abundant materials, such as metals phosphides, carbides, transition metal dichalcogenides and selenides have been studied extensively for OER over the past few years. In this case, Hydrogen is considered is to be one of the most suitable and capable for the production of energy. Because hydrogen is abundance and big advantage is that, there is no greenhouse gases during the consumption for the production of energy and it is renewable energy source. Hydrogen can be produced in different ways, like biomass, fossil fuels and electrolysis of water with the help of electricity. Energy efficiency and its impact on environment depends on the way of the production method of hydrogen. Different method has been used for the production of hydrogen, like Fermentation, Gasification or Reforming and Electrolysis. Moreover, there are advanced techniques f includes Photobiological water splitting, High temperature and Photoelectrochemical water splitting.

Electrochemical water splitting is the most suitable technique rather than wind energy and solar energy for the generation of pure hydrogen. Electrolysis f water having large resistance of Polarization, slow moving kinetics of anodic and cathodic reactions and over potential produced by them. Electrolyzer that are used in commercial required operating potential ranging (1.8-2V) that is far greater than the anticipated value of (1.23V). As a result, we must overcome the slow behaviour of OER and ORR processes, which are aided by the use of precious metal electrocatalysts, which boost catalyst activity, durability by increasing active spots and increases electro-conductivity. Pt/C is the most active metal for oxygen reduction reaction, however, due to the development of platinum oxides in the form of a surface coating at higher potentials, its activity for oxygen evolution process reduces. Contrary to this, for the OER process, RuO_2 and IrO_2 have the greatest catalytic activity. So that due to these problems and mainly cost issue of precious or expensive metals assisted the

electrochemist to move from precious metals catalyst to non-precious metal catalysts which are simultaneously active for both type of reactions which have mentioned above but stability and corrosion to electrodes diverted scientists attention towards exploring nonprecious electrocatalysts that can enhance the catalytic activity of electrochemical reactions involved in water splitting. Perovskites has been used in different forms as an efficient and cheaper catalyst, but our major concern is to develop a composite of perovskites with 2D material properties. The research is about developing a nanostructured STF based double perovskites electrocatalysts by doping of praseodymium Pr in Sr_2TiFO_6 (STF) based double perovskites for the mechanism of water splitting processes with catalytic activity and stability comparable to that of state-of-the-art Pt. Perovskite will be prepared by EDTA Complexing Sol-Gel method. We will be prepared perovskite material by doping different amount of praseodymium Pr metal of lanthanoid series in STF double perovskites. The research phase will be based on studying the Structural properties and Electrochemical properties.

1.1. Mechanism on the catalyst surface

1.1.1. Electrochemistry of water splitting

The catalyst is applied on anode and cathode where it assists in carrying out OER and HERs, by speeding up the water splitting mechanism[28]. The reaction can occur in an alkaline media or an acidic media with the given mechanism as follows[29, 30]

In anodic solution

At cathode

$$2H^+ = 2e^- \rightarrow H_2 \tag{1}$$

At anode

$$H_2O \rightarrow 2H^+ + \frac{1}{2}O_2 + 2e^- \tag{2}$$
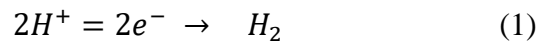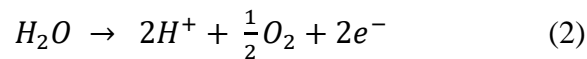
In neutral or alkaline solution

At cathode

$$2H_2O + 2e^- \rightarrow 2OH^- \tag{3}$$

At anode

$$2OH^- \rightarrow H_2O + \frac{1}{2}O_2 + 2e^- \tag{4}$$

5
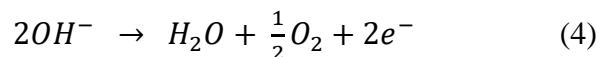
Alkaline electrolytes, in comparison with acidic electrolytes, allow precious metal catalysts such as platinum, Iridium, or ruthenium, to be substituted with inexpensive transition metal and/or functional carbon-based catalysts[31].
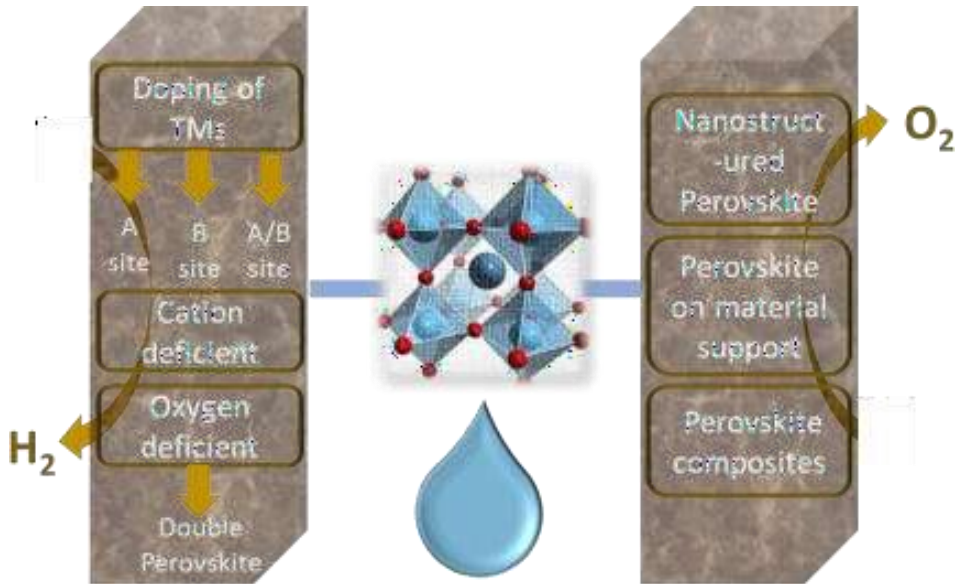
Figure 2: Schematic overview of different perovskite catalyst used for water splitting reaction of HER and OER [2]

1.1.2. Hydrogen Evolution Reaction Mechanism

In alkaline medium, the whole HER works at a standard voltage of -0.829 V. In general, the HER process consists of 3 stages, each of which is processed by one of 3 types of reactions such as Tafel, Heyrovsky and Volmer reactions, Eq. 5-9 in acidic and alkaline environments. They're listed below[2, 32]

Volmer Reaction (adsorption electro chemically) (Eq. 5-6)

$$H^+ + * + e^- \ \rightarrow \ H* \quad \text{(in acidic medium)} \tag{5}$$

$$H_2O + * + e^- \ \rightarrow H^* + OH^- \quad \text{(in alkaline medium)} \tag{6}$$
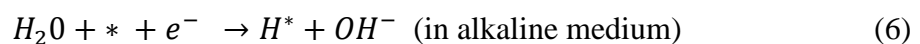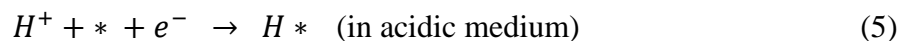
Heyrovsky reaction (desorption electrochemically) (Eq. 7-8)

$$H^* + H^+ + e^- \ \rightarrow * + H_2 \quad \text{(in acidic medium)} \tag{7}$$

$$H^* + H_2O + e^- \rightarrow * + H_2 + OH^- \text{ (in alkaline medium)} \qquad (8)$$
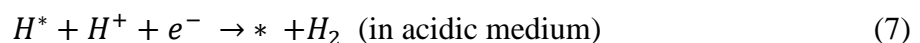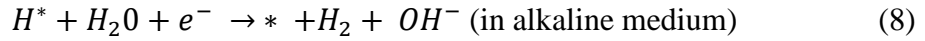
Or Tafel reaction (desorbed chemically) is expressed in Eq. 9

$$2H^* \rightarrow 2 * + H_2 \qquad (9)$$

Heyrovsky and Tafel stages involving the molecular adsorption of H₂O molecules across the bared active sites use Volmer reaction pathways. After that, the electrochemical reduction of water molecules takes place that have become adsorbed on the active site into H* and OH, this results in OH desorption and, eventually, the hydrogen molecule leaving the surface. For perovskite oxide catalyst, a mechanism has been proposed, which shows that the catalyst does not have a metal reactive site and instead relies on a negatively charged surface oxygen. Xu et al. presented a mechanism showing alkaline HER steps, given in Figure 3. [33]. It is explored if Pr0.5 (Ba0.5Sr0.5) 0.5Co0.8 Fe0.2 O3– δ perovskite oxide is effective in catalyzing HER. The process states that a water molecule accessible from electrolytes and electrons interacts with an active site occupied by oxygen to form an intermediate known as adsorbed H*, in which the metal sites in the vicinity are either reduced or increased (with oxidation states ranging from n+1 to n). Though the involvement of the second phase (Heyrovsky reaction or Tafel reaction) is difficult to predict, OER/ORR yields a variety of reaction intermediates. However, because only one intermediate is produced during the two-electron transfer HER, extremely active catalysts (e.g., Pt) have negligible overpotential, indicating the need to enhance perovskite catalysts [34]. The H* intermediate's binding potential, which is typically provided free energy for hydrogen adsorption (ΔGH), determines the HER rate [35]. The effectiveness of the HER catalyst is determined by its hydrogen binding ability, which should be moderate, not too strong nor too weak, with a GH value near to zero.
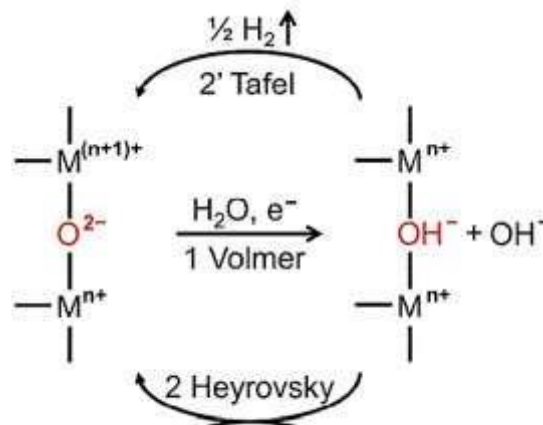
Figure 3 :Mechanism proposed for HER on the surface of perovskite oxide [12]

1.1.3. Oxygen evolution reaction OER /ORR reaction mechanism

Tseung and Jasem [62], in 1977 introduced the concept, at lower potentials than the oxygen electrode if transition metals were connected with redox electrodes, more active sites would be generated with greater levels of oxidation. As a consequence, an excellent catalyst was developed with an active OER/ORR catalyst as well as improved electrical conductivity. Trasatti [36, 37] between 1980 and 1988, he studied oxides of perovskite-type. Meanwhile, Otagawa and Bockris [38, 39] studied eighteen different perovskite oxides and discovered that when tested under constant overpotential, The enthalpy of $M(OH)_3$ hydroxide generation is inversely proportional to current density.

Man et al. [40] offered a modification to the mechanism that had been proposed previously. A Lewis base (a metal-bound electrophile) attacked by an oxygen nucleophile (OH^-) involving in a process, depicted in Fig. 3, as a sequence of acid-base reactions [62]. The ORR reaction can be written as ($O_2 + 2H_2O + 4e^- \rightarrow 4OH^-$) in alkaline solution [59], whose 0.401 V is the standard electrode potential. At metal sites, the reaction occurs by a four-step proton coupled mechanism [41]. The reactions are carried out in the following order: 1). Hydroxide displacement; 2). Peroxide formation; 3). Oxide formation; and 4). Regeneration of hydroxide as shown in (c). To create oxygenated products, the first stage includes the reaction of H_2O or molecular O_2 with metal surface sites, denoted by the letters OH*, O*, OOH*, and OO* where '*' represents a catalytic surface reactive site. The surface metal sites' oxidation and reduction (redox) are accompanied by the oxygenated adsorbates having oxidation state between n+1 and n+. The quantity of oxygen bound and the number of surface metal sites determined the kinetics of ORR. The transition from OH* to OO* is said to be the rate determining step (RDS) for oxygen when the binding energy of oxygen is sufficiently high, whereas the transfer from O* to OH* is said to be the rate limiting step when the oxygen binding energy is too high. An ideal perovskite catalyst, according to the Sabatier principle, has a modest binding energy of oxygen [41],[42]. Suntivich et al. [43] claimed that the rate-determining stages are greatly affected by the orbital filling in metal cations, claiming that if filling is greater than 1, the the O-O bond creation in the OOH* adsorbate would really decide the rate. While the creation of peroxide ions from oxyhydroxide can be a rate determining step (RDS) for less than 1. With the removal and regeneration of OH-, OER has a similar process.

In an alkaline medium, the reaction on the perovskite surface for OER may be expressed as $4OH^- \rightarrow O_2 + 4e^- + 2H_2O$, which goes through the following four phases in order:

i. Hydroxide deprotonation
ii. Peroxide formation
iii. Peroxide deprotonation
iv. Hydroxide formation

The oxidation state altered from n+ to n+1 by causing redox reactions on metal surfaces when the electrolyte's OH$^-$ reacts with metal sites. OH*, OO*, OOH* and O* are the reactive intermediates in order. The degree of oxygen binding to metal sites also influences the reaction kinetics of OER. The rate limiting step, when oxygen bonds insufficiently, is represented by peroxide generation (O* to OOH*). In the deprotonation step (OOH* to OO*), it acts as a rate determining step when oxygen bonds too tightly [73]. Due to scaling relations, The surface oxygen adsorbate binding strength in OER and ORR is highly interrelated, allowing for the calculation of nonzero overpotential for many reported perovskites.

Chapter 2

Literature Review

In rechargeable air-metal batteries, fuel cells, chlor–alkali cells, water electrolyzers, and CO_2 reduction, oxygen reduction and evolution are critical electrochemical processes. The kinetics of these processes provide a significant barrier in terms of putting these technologies into practice. The use of electrocatalysis to assist the oxygen reduction process (ORR) has been a prominent research issue, and great advancements have been achieved experimentally in this area in the hunt for cheap, highly active catalysts. In 1950s and 1960s, to better understand the oxygen evolution reaction's mechanics, extensive research was conducted on several catalyst materials [44], although the ORR received the most attention, as evidenced by the number of publications. However, efforts to enhance OER using better and low-cost catalysts have lately reawakened interest.

The OER's sluggish kinetics is a key subject in electrocatalysis, and therefore in water electrolyzers, H2/O2 fuel cells and air-metal batteries, restricting their efficiency by more than 15% owing to power losses [45]. Previously, noble metals (for example, Pt, Pd, Ir, and Ru) and their alloys were the only electrocatalysts available for the OER. Later research revealed that the presence of a thick oxide coating on the noble metals' surfaces was responsible for the enhanced OER [46]. As a result, in the development of OER catalysts, the utilization of different mixed oxides is a key focus. This comprises catalysts made from a combination of IrO_2 and Pt [47], IrO_2 and TiO_2 mixes [48], IrO_2 and SnO_2 mixtures [49, 50], IrO_2 [34, 51], RuO_2 [52], and a combination of both. Precious metals, on the other hand, have relatively high prices for large-scale applications, restricting their practical usage. As a result, research has concentrated on lowering or eliminating the usage of precious metals in electrocatalysts.

2.1. Perovskites Electrocatalysts

Transition metal oxides, which are very inexpensive, have been investigated as a possible alternative for precious metal-based products. MnO_2[53], $NiCO_2O_4$ [54], $La_1xSr_xMnO_3$ [55], $La_1xSr_xCoO_3$ [56], and $La_1xMn_xCoO_3$ [57] were among the compounds studied. Perovskite-type oxides are well-known for their usage in high-temperature solid oxide fuel cell (SOFC) [58], but they've also been used for OER in

alkaline media [59]. Since the earliest papers on OER, their electrocatalytic actions toward OER have been investigated to some extent [60], and they have rekindled attention in recent years [61-66]. Different theoretical descriptors have been used to rate the activity of various perovskite materials for OER and ORR in so-called volcano plots [67].

Perovskite's exhibit metallic conductivity and even semi conductive due to their non-stoichiometric composition and chemical structure (ABO3). Furthermore, their catalytic and physicochemical characteristics can be altered because ions of the different or same oxidation states can be substituted in the A and B sites [68]. As a result, perovskites are promising materials for fundamental electrocatalysis research aimed at establishing links between electrocatalytic and physicochemical characteristics.

The ability of perovskite oxides to be engineered as an excellent electrocatalyst for oxygen evolution reaction (OER) as well as hydrogen evolution reaction (HER) is garnering traction as a requirement for developing reversible rechargeable air-metal batteries and fuel cells. To determine the inherent increase in activity of each reactive site, one method is to account for the perovskite electronic structure's physicochemical characteristics including a wide variety of compositions produced via oxygen vacancies, substitution, and a variety of crystal shapes. Extrinsically increasing the number of reactive spots and activity, which is a function of geometric impact, is the second option. By inventing novel methods for manufacturing perovskite nanostructures and composites, this can be done. These variables are intertwined, and altering one of them can have an immediate effect on crystal structure as well as the oxygen vacancy. For example, in some instances, both intrinsic and external characteristics might increase at the same time [69].

2.2. Composition of perovskites

Through changes in the electronic structure, the substitution of A-site/ B-site components have a considerable influence on catalyst's activity. When a transition metal and rare earth metal are combined, the net absolute charge addition at the A-site by the metal cations changes. This affects the transition metal cations' spin state as well as changing the oxidation state, perhaps resulting in an oxygen vacancy [15]. The majority of the study has focused on comparing the characteristics between transition

metals doped at B-site and rare earth metals doped at A-site. Starting with the A-site dopant catalyst's findings in terms of doping at both the B and A sites.

2.2.1. A-site Doping

The perovskite oxides' catalytic activity influenced by many variables, with the perovskite oxides' A-site cations playing a key role in catalytic activity. To begin with, the crystal structure will vary due to the various A sites' cation radii. The octahedron will tilt due to the A-site ion' electronegativity, and varying degrees of tilting result in distinct crystal fields, which result in varied optical and electrical characteristics. Meanwhile, because the A–O interactions may change the B-site cations' redox energies, inside perovskites the A-site cations play a key role in regulating the activity of oxygen reduction reaction (ORR). The B–O distance rises somewhat as the A-site cation's radius grows for a constant B oxidation state, which may encourage an optimum electronic B-sites' configuration for the four electron ORR. Furthermore, because of the states' density near the Fermi level contributed by the A-site cations' 4f electron, the A-site cations can impact electronic conductivity.

Second, the insertion of A-site deficit causes the lattice to expand owing to an optimization of the occupancy and increase in oxygen vacancies of the B-site transition metal, in the oxygen evolution process, this significantly improves catalytic activity. Finally, adjusting the A-site ions' stoichiometry can effectively modify the B-site ions' valence and concentration of oxygen vacancy. Because of their potential for practical application, it's worth keeping an eye on fresh findings in rare-earth metal perovskite oxides or A-site inhabited alkaline-earth [70]. By controlling the A-site cations' size, the perovskite oxides' physical characteristics as well as crystal structures may be successfully manipulated [71]. For various applications, creating as well as designing alternative A-site cations, inserting defects and doping/ substitution, at A-site perovskite oxides to increase the catalytic activity is important. On the perovskite oxides' performance and structure influenced by various A-site cations has not yet been explored in the literature. Furthermore, with the different perovskite oxides' creation, A-site perovskite oxides have made tremendous progress in recent years. As a result, it's worth looking at the A-sites' role in perovskite oxides.

Lanthanum has been widely employed as an A-site element in the production of rare earth metals. Depending on the stoichiometry and technique of production, A-site

doping obviously improves catalytic activity. Shao et al.[72] experimented with strontium-based lanthanum La1xSrxFeO3-δ (x = 0, 0.2, 0.5, 0.8, and 1) perovskite catalysts and in alkaline solution, found the one with the highest OER activity. Because Fe^{2+} is oxidized to Fe^{3+} and charge is compensated when Sr^{2+} replaces La^{3+}, increasing Sr doping lowers the lattice size directly. Gao and Jin [17], who synthesized an urchin-like La0.8Sr0.2MnO3 (LSM) perovskite with urea precipitator by co-precipitation technique for OERs and ORR, showed a highly unusual structural strontium doped perovskite because Sr doping improves activity. LSM's large specific surface area, LSV findings for OER, as well as high density of cathodic current (3.7 mA cm^{-2} at 0.9 V (vs. AgCl/Ag)) influenced bifunctional catalytic activity significantly. The sphere's diameter was 3-5 µm, while the thorns' length was 0.2-0.6 µm. The first-order kinetics of O2 and dependence on the succeeding electrocatalyst for applied potentials were represented by parallel and linear graphs in Urchins like LSM [59]. Tulloch et al. [84] made a similar contribution, working on perovskite type of La1xSrxMnO3 for even values of X (0-1) and finding La0.4Sr0.6MnO3 to take the lead in the process of oxygen reduction. It was observed that the catalyst was modest surface area ($<1m^2\ g^{-1}$), very crystalline and with a high.

2.2.2. B site doping

For the oxygen evolution reaction and oxygen reduction reaction, introduce a completely noble-metal-free, economical, stable, and particularly active bifunctional electrocatalyst based on CaO-doped NdBaCo2O5+δ for the oxygen electrode with the goal of exploiting its activity of high catalytic. The electrochemical performance of the NdBa0.75Ca0.25Co2O5+δ electrocatalyst, that was enhanced with the help of doping oxides of transition-metal such as Mn^{2+}, Cu^{2+}, Ni^{2+} and Fe^{2+} into the double perovskite oxides' B-sites, allowing oxygen-ions and electrons to flow via vacancies of oxygen. For the ORR and OER, NdBa0.75Ca0.25Co1.5Fe0.5O5+δ has the greatest activity of electrocatalytic oxygen electrode, thus to increase its endurance and catalytic activity, it is hybridized with nitrogen-reduced graphene oxide (N-rGO). The activity of bifunctional oxygen electrode (0.761 V) increased by NBCCFe's hybridization with N-rGO while also improving outperforming of catalysts such as C/Pt (0.815 V), durability and C/Ir (0.768 V). The increased discharge reduced longer cycle life, charge overpotential and capacity of a rechargeable battery (lithium–air) built with the catalyst such as N-rGO/NBCCFe corroborates the N-rGO/NBCCFe's

outstanding bifunctional catalytic activity. The catalyst such as N-rGO/NBCCFe also exhibits the finest polarization during charge and discharge, suggesting the greatest bifunctional catalytic activity [73].

2.2.3. A/B site Doping

Surface roughness and active site availability are increased by doping transition metals and rare earth metals. In this situation, more in-depth research is required to determine the best composition for increased activity. The chosen technique alters the structural characteristics of the doped material depending on the doping method used. For developing the quaternary perovskite catalyst, several techniques have been presented, each with various catalytic structure and characteristics. On a strontium doped perovskite, Singh et al.[74] investigated the effect of replacing transition metals in $La_{0.8}Sr_{0.2}Co_{1-y}$ by O_3, where B might be Cr, Ni, Fe and Cu. The electrocatalytic properties of the following catalysts were studied, and a pair of redox peaks were identified using CV before the start of OER. The use of transition metals at the B-site resulted in a substantial increase in surface roughness, resulting in a high active surface area.

Because of its excellent charge transferability, barium-based strontium doped cobalt iron perovskite oxide has been investigated for many years. $Ba_{0.5}Sr_{0.5}Co_{0.8}Fe_{0.2}O_{3-\delta}$ (BSCF82) was found by J. May et al. [75] to be the most effective catalyst in an alkaline solution for water oxidation. The researchers used HRTEM to investigate the changes and stability in surface morphology for a variety of catalysts that occur during OER, including catalysts such as BSCF82, $La_{0.4}Sr_{0.6}CoO_{3-\delta}$ (LSC46), $LaCoO_3$ (LCO) and $LaMnO_3$ (LMO). The activity of OER decreases as the cobalt atoms' cluster size grows larger [75]. The electrochemical behaviour of $Ba_{0.5}Sr_{0.5}Co_{0.8}Fe_{0.2}O_3$ (BSCF) was investigated by Gao and Jin [59] in the same region, but with a different rare earth element stoichiometry (x=0.5) . Its use in alkaline medium as a bifunctional catalyst (ORR and OER) has been confirmed. The catalyst's limiting current density is equal to 20 wt% C/Pt. However, when compared to Gao and Jin's study, the BSCF perovskite catalyst's onset potential is lower than the C/Pt catalyst. This is due to the BSCF perovskite catalyst's diffusion limiting current density. This is because the electrocatalyst has a variety of O2 interactions as well as the adsorption of various species on transition metal cations. When employed in an alkaline medium, BSCF can thus be regarded a potential bifunctional catalyst [59].

The use of large oxygen vacancies to substitute Pr in oxide of BSCF perovskite-type investigated by Bu et al. [8], which displays greater stability and strong electrical conductivity, to investigate the influence of other rare earth metals such as perovskite structured Pr-doping. The ORR/OER activity is significantly increased when the cobalt's oxidation state is higher and there are more oxygen vacancies. Within a potential range of 0.3-0.6 V, it showed a high transfer number of electron such as 3.77-3.89. In a charge-discharge curve, it also exhibited better cycle stability, indicating that OER/ORR has a bright future.

Chang et al. [76] using ruthenium as the B-site dopant, created a very stable substituted perovskite structure and reported $La_{0.6}Ca_{0.4}Co_{0.8}Ru_{0.2}O_3$ powders produced by the amorphous citrate precursor technique for ORR. With pore sizes ranging from 0.5 to 3.0 μm, a foam-like microporous structure is produced. This catalyst's enhanced catalytic activity in the KOH solution, due to a greater deposition rate of hydrogen peroxide. The results for the polarization curve of $La_{0.6}Ca_{0.4}Co_{0.8}Ru_{0.2}O_3$, $La_{0.6}Ca_{0.4}Co_{0.8}Ru_{0.2}O_3$/BP2000 (black pearl 2000), and $La_{0.6}Ca_{0.4}CoO_3$/ BP2000.

2.2.4. Double Perovskites

Environmental technologies and clean energy are required for a sustainable future. High-performance catalysts are at the heart of these technologies, allowing them to enhance the critical chemical processes' selectivity and pace. With a straightforward atomic structure, single perovskites have long been thought of as an active catalyst's type [77-79]. Cation ordering characterises double perovskites, a subclass of perovskites, are gaining popularity as feasible replacements for single perovskites, with performance equivalent to or greater than single perovskites. The production of a doped single perovskite $A_{1-x}A'_xBX_3$ (or $AB_{1-y}B'_yX_3$) is often achieved by replacing cations, in which the cations A and A' (or B' and B) are arranged in a disorderly pattern, A-site (or B-site) cation ordering may arise if x (or y) 0.5 and A' and A (or B' and B) cations are sufficiently distinct in charge and size [80-82]. The result is a compound known as a double perovskite, with the formula $AA'B_2X_6$ (or $A_2BB'X_6$). Both B-site and A-site ordered double perovskites can be arranged in 3 distinct ways (columnar, layered, or rock-salt), the most frequent being A-site layered and B-site rock-salt ordering [83, 84].

The development of a double perovskite structure can improve the efficiency in relevant applications, physicochemical characteristics of the material, stability, and impacting activity [85, 86]. Firstly, double perovskites increase the perovskite family' compositional space by allowing atoms that would otherwise be unable to accept in single perovskites (for example, high valence elements like 6+, 7+) [87, 88]. Secondly, atomic environments in double perovskites are more complex than in single perovskites, which can result in electronic configurations not observed in single perovskites. Because oxygen vacancies are localized in the AO plane, A-site ordered oxide double perovskites $(AA'B2O5+\delta)$ have alternating layers of |AO|BO2|A′O|BO2| and hence have two symmetries for B-site cations (for example, square pyramidal and octahedral) [89]. Two elements in the corner-linked, alternating B′X6 and BX6' octahedra are anticipated to operate in a more complimentary way with B-site ordering in double perovskites, contributing to substantially enhanced chemistry. Third, the performance of double perovskites is considerably improved. chemical stability in catalytic settings, such as strong basic/acidic solutions and strongly oxidizing/reducing atmospheres, and heat, humidity, light, or CO2 [29, 90-93].

Table 1: Some of the most advanced bifunctional catalysts have been described in alkaline media for their activity and endurance. BI between -1 mA cm-2 and 10 mA cm-2.

Catalyst	ORR (V) @ -1 mA cm^{-2}	OER (V) @ 10 mA cm^{-}	BI (V)	Stability	Ref.
O$_2$Ru	~ 0.82	~ 1.62	~ 0.8	discharge performance and a stable potential battery	[94]
N- CNT/ Co$_{0.2}$La$_{0.58}$Fe$_{0.8}$O3Sr$_{0.4}$	0.813	1.639	0.826	Stable after 25 hours	[95]
LaCoO3/NC	0.83 V	1.66	0.83	Stable to 100 OER and 200 ORR cycles.	[95]

FeN_X-C/ La$_{0.58}$ Fe$_{0.8}$O$_3$Sr$_{0.4}$Co$_{0.2}$	0.82	1.68	0.86		[94]
N- CNT/ Sr$_{0.4}$Co$_{0.2}$Fe$_0$La$_{0.6.8}$O$_3$	0.72	1.60	0.88	Stable results after 40 hours at current density of 10 mA cm^{-2}	[96]
C/ Co$_{0.8}$Fe$_{0.2}$ O$_{3-\delta}$ La$_{0.7}$(Ba$_{0.5}$ Sr$_{0.5}$)$_{0.3}$	0.72	1.6	0.88	Stable during 100 cycles of discharge/charge at air-Zn full -cell.	[97]
NC/LaNiO$_3$	~0.88	~1.78	~0.9	In the region of 0 to 1.98 V, it is stable to cyclic voltammetry.	[98]
C/ 0.7Co$_{0.8}$O$_{3-\delta}$Fe$_{0.2}$ La$_{0.3}$(Ba$_{0.5}$ Sr$_{0.5}$)	~0.7	~1.63	~0.93	Under O2, stable to ORR for 30000s at 0.345 V.	[99]
Hierarchical mesporous-macroporous La$_{0.5}$Sr$_{0.5}$CoO$_{3-\delta}$	~0.7	~1.64	~0.94	In a LiO2 battery, excellent cycle stability was achieved after 50 cycles at 0.1 mA cm2.	[99]
N-CNT/Co-doped LaMnO$_3$	~0.824	~1.784	~0.96		[100]
Fe$_{0.2}$O$_3$LaNi$_{0.8}$	0.694	1.714	1.02	The presence of NiO on the surface causes degradation under ORR. 300 OER cycles of stability	[101]

Catalyst	ORR	OER	BI	Stability	Ref.
N-CNR/LaTi$_{0.65}$$_{35}O_{3-\delta}$ NP Fe$_{0.}$	0.78	1.81	1.03	At 5 Ag-1, the charge-discharge curve is stable.	[102]
N-rGO/ La$_{0.58}$ Co$_{0.2}$Fe$_{0.8}$ Sr$_{0.4}$O3-δ NR	0.67	1.72	1.05	DURING THE 18000S, THERE WAS A 10% DECREASE IN ORR ACTIVITY AT 0.624 V. .	[103]
FeO$_{3-\delta}$ La$_{0.95}$	0.58	1.64	1.06		[104]
Mesoporous La$_{0.5}$Sr$_{0.5}$CoO$_{2.91}$ NW	0.78	1.84	1.06		[105]
La$_{0.6}$CoO$_{3-\delta}$Sr$_{0.4}$	0.755	1.835	1.08	Li–air battery discharge-charge curves: At 0.1 mA cm^{-2}, it was stable for 50 cycles.	[106]
C/Y$_2$(Ru$_{2-x}$Y$_x$)O$_{7-\delta}$	0.54	1.64	1.10		[107]
La Mg$_{0.15}$O$_3$Ni$_{0.85}$	0.714	1.864	1.15		[108]
C/BaTiO$_{3-\Delta}$	0.38	1.70	1.32		[104]

Table 2: Activity and durability of some of the state-of-the-art bifunctional catalysts reported in alkaline media. BI between -3 mA cm^{-2} and 10 mA cm^{-2}.

Catalyst	ORR (V) @ -1 mA cm^{-2}	OER (V) @ 10 mA cm^{-}	BI (V)	Stability	Ref.

AB*/La$_{0.8}$ MnO$_3$Ca$_{0.2}$	0.892	1.564	0.672	Zinc-air batteries that can be recharged. At 10mA cm-2, the charge-discharge cycle is stable for 10 hours.	[109]
N- rGO/ Nd$_{1.5}$ CoFeMnO9−δ Ba$_{1.5}$	0.889	1.587	0.698	ORR/OER: stable after 10 h at -3 mA cm^{-2}. & at 5 mA cm^{-2} respectively.	[110]
AB*/La$_{0.7}$ MnO$_3$Ca$_{0.3}$	0.873	1.593	0.720		[104]
AB*/La$_{0.6}$ MnO$_3$Ca$_{0.4}$	0.85	1.633	0.783		[103]
AB*/La$_{0.9}$Ca$_{0.1}$MnO$_3$/	0.858	1.651	0.793		[111]
C/Pt	0.894	1.695	0.801		[108]
KB /Pd	0.84	1.68	0.837		[108]
KB/Pb$_2$Ru$_2$O$_{6.5}$	0.81	~1.65	0.84	AFTER 1500 S AT 0.7 V, THERE WAS A 30% REDUCTION IN ORR ACTIVITY. After 1500 seconds at 1.5 V, there is a 20% reduction in OER activity.	[112]
NC/Ba$_{0.5}$ Fe$_{0.2}$O3-δ Sr$_{0.5}$Co$_{0.8}$	0.74	1.58	0.84	Stable results after 1000 cycles	[95]

CB/ PrBa$_{0.85}$Ca$_{0.15}$MnFeO$_{5+\delta}$	0.77	1.64	0.887	After 12 hours at E1/2, there was a 5% loss in activity (ORR). After 12 hours at 5 mA cm2, it is stable (OER).	[113]
KB/La$_{0.6}$Co$_{0.2}$O$_3$Sr$_{0.4}$Fe$_{0.8}$	0.77	1.65	0.883	At 80 mA cm-2, stable for 2000 charge-discharge cycles	[114]

Chapter 3
Material and Methods

3.1. Materials:

The material purchased for preparation of STF and STF/Praseodymium doped electrocatalysts was analytical-grade $Sr(NO_3)_2$ (98%, Alfa Aesar, UK), $C_{12}H_{28}O_4Ti/Ti[OCH(CH_3)_2]_4$ (titanium isopropoxide[TTIP]) (97%, Sigma, USA), $Fe(NO_3)_3.9H2O$ (98%, Alfa Aesar, Belgium), and $Pr(NO_3)_3$ as metal precursors, they were employed. To start the combustion process, glycine (99.7%, VWR chemicals, Belgium) was employed as a chelating agent and fuel. Without further purification, all reactants were utilised as supplied.

3.2. Synthesis of STF double perovskite

The precursor solution was made by dissolving metal nitrate salts in deionized water in stoichiometric quantities of Fe and Sr such 1:2 respectively, then TTIP was dissolved in ethanol at room temperature. For three hours, both solutions were agitated separately before being combined together. Then, after mixing the two solutions together (Fe and Sr salts dissolved in H_2O and TTIP dissolved in ethanol), glycine powder was added to the resulting solution. The stoichiometric quantity of glycine necessary was determined using propellant chemistry principles such as valences of reducing and oxidising elements. The calculations were done using standard valences for metallic nitrates, such as +2 for Sr and +3 for Fe, and valences for common elements, such as 0 for N, +4 for Ti, +1 for H, +4 for C and -2 for O. For example, Sr$(NO3)2$ had a valency of $+2 + (0 -2\times3) 2 = -10$, but glycine ($C_2 H_5 NO_2$) had a valency of $(+4\times2) + (1\times5) + (0-2) \times 2 =+9$. To create STF powder, the best metal cation to stoichiometric glycine ratio necessary is 1:2, according to these calculations. A heated plate was used to evaporate the combination of the two solutions, a thick gel was formed when constantly agitated at 90°C.Then, 300ºC temperature of hotplate raised, causing the gel to self-ignite and the production of black STF ash. In a preheated oven, the self-combusted gel was then dried for 12 hr at 120°C. The dried black ash at 900°C for 3 hours was calcined in the air to get pure black double perovskite STF powder. (Magma Therm, Model: CWF1200, Turkey).

Sr (NO$_3$)$_3$.6H$_2$O ➕ Deionized Water ➕ Fe(NO$_3$)$_2$.9H$_2$O ➕ Titanium isopropoxide

STF

Deionized water

Pr(NO$_3$)$_2$.6H$_2$

After mixing of 3 hrs. at room temperature

Suspension Evaporation at 80°C

Mixing at room temperature for 5 hrs.

Calcination at 850 °C

Pr doped STF Catalyst formation.

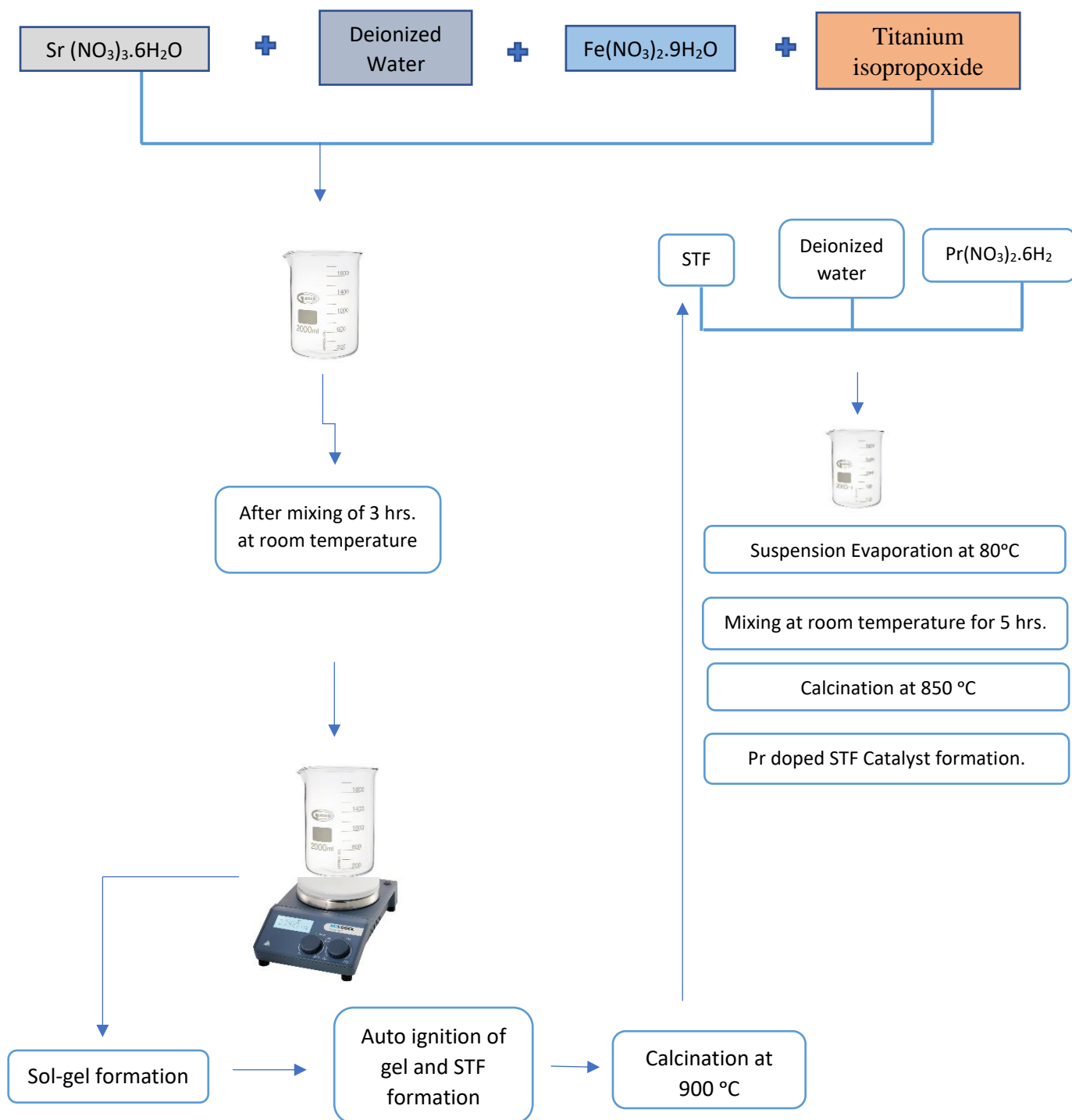Sol-gel formation → Auto ignition of gel and STF formation → Calcination at 900 °C

Figure 4: Schematic diagram of synthesis of STF based electrocatalyst

3.3. Synthesis of STF electrode

The ink was made by dissolving 10mg STF in 500LμL DI water, 450μL isopropanol, and 50μL Nafion, then sonicating it for 45 minutes in a sonication bath. A mass loading of about 2-3 mg cm^{-2} of powdered LSTN ink achieved when placed on dried Ni foam. Ni foam was dispositioned, dried, and weighed.

3.4. Characterization Techniques

3.4.1. X-ray Diffraction (XRD)

The crystalline nature of (Sr2TiFO6) STF based double perovskites material was evaluated by STOE-Germany X-ray Diffraction. A voltage of 40 kV and a current of 40 mA were used in the experiment. The sample was scanned using a step size of 0.04 and a step time of 0.5 seconds per step. The scan angle was varied between 2θ (10° to 80°). CuKα radiation had a wavelength of 1.540Å.

The average crystallite size was determined using the following Debye-Scherrer Equation:

$$\tau = \frac{0.9 \, \pi}{\beta \cos \theta} \cos \theta$$

X-ray diffraction is used to analyze the atomic spacing and crystal structure.

Objectives of XRD

The objectives of XRD are**:**

  i.   It identifies of crystallinity of material

 ii.   It is used to distinguish between crystalline and amorphous forms

iii.   To calculate the lattice spacing of material.

 iv.   To find out average particle size

Working Principle

The XRD works on constructive interference between monochromatic X-rays. Cathode ray tube produce X-rays which are then filtered to generate monochromatic radiations. To focus the rays towards specimen, these rays are concentrated by collimation. The interaction between these rays and specimen results constructive interference, which satisfy Bragg's Law. Bragg's Law states the direct relation of

wavelength of the electromagnetic radiations with lattice spacing and diffraction angle of the specimen. It can be written as

$$n\lambda = 2d \sin \theta$$

Where,

n = order of reflection,

λ = wavelength of X-rays,

d = specimen's typical gap between crystal planes.

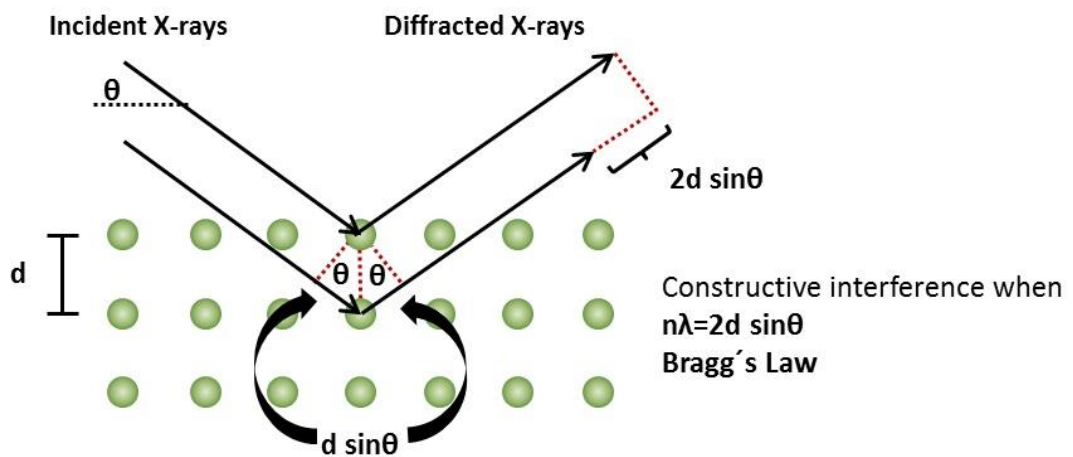θ = angle produced by the incident beam and the lattice plane's normal.

Figure 5: Schematic diagram of XRD principle [35]

3.4.2. Fourier Transform Infrared Spectroscopy

The interfacial interactions between two phases via composite synthesis were studied using FTIR. For the analysis, the Fourier Transform Infrared Spectroscopy (ATR-FTIR, BRUKER) equipment was employed. The study was performed with a scanning frequency of 32 and a resolution of 4 cm^{-1} in the range of 4000-500 cm^{-1}.

Objectives of FTIR

The objective of FITR is to

i.   Recognize organic, polymeric or sometimes inorganic compounds
ii.   Characterization of unknown materials
iii.   Identification of contaminations (in or on the materials)
iv.   In failure analysis, identify decomposition, oxidation or uncured substances

Working Principle

The FTIR works on absorbance of light by molecules, while they are in infrared region of the electromagnetic region. The absorption of light uniquely implies to the bonds present in the molecules. The infrared region lies within range of 12800 to 10 cm-1, which is further divided into near, mid and far infrared regions

Infrared region	Range of Frequency
Near IR	1280-4000
Mid IR	4000-200
Far IR	1000-50

Infrared absorption spectrum mechanism is based on vibrations of molecules. When the specimen is exposed to radiations, its molecules absorb radiations of certain wavelength. This changes the dipole movement of specimen molecules. As a result, the energy level of the specimen molecule is transfer to excited state from the ground state. The energy gap determines the frequency of absorption peak. The change in intensity is subjected to the dipole moments and shift of energy levels.

Components of FTIR

The basic components of FTIR are

i.   Source

ii.   Interferometer

iii.   Sample compartment

iv.   Detector

v.   Amplifier

vi.   A/D Converter

vii.   Computer

The radiations are generated by the source. These radiations after passing through the interferometer reaches the specimen and are recognized by the detector. The signals are amplified by means of amplifier using analog-to-digital converters that convert analogue signals to digital signals. Finally, the signal is sent to a computer, which performs the Fourier Transform.

3.4.3. Ramon Spectroscopy:

It is a molecular spectroscopic technique that uses light to interact with specimen and give characteristic information. It obtains information about the spectrum of individual vibrations of a molecule by scattering light rather than absorption of light, like FTIR does. It also provides information about vibrations and lower frequency modes, which are very useful to det brief understanding of crystal lattice and basis of molecular structure.

Working Principle:

The light interacts with the molecules available in solid, liquid or gas, the photons within incoming light get dispersed with same energy as that of incident photons,
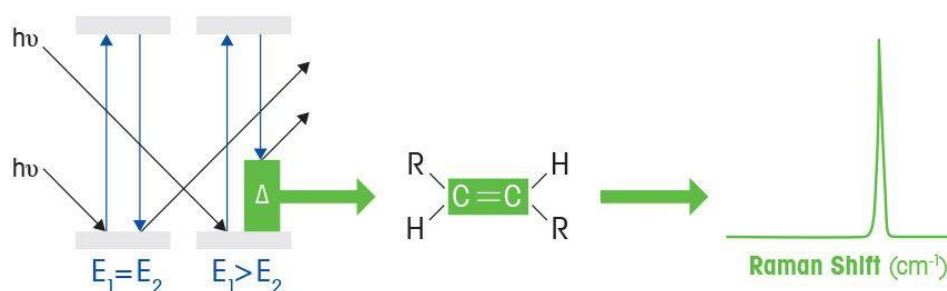

Figure 6: Working principle of Raman spectroscopy [19]

thereby undergoing elastic scattering. Only a small number among them undergo inelastic scattering. Raman helps user to capture vibrational characteristic signature of molecule, that develops an understanding of how they are put together as well as their method of interaction with other molecules around it.

3.4.4. Scanning Electron Microscopy (SEM)

The morphology of perovskites and its composites were recognized by SEM (JSM64900). Prior to analysis, powder of material was placed on stud and gold plated to provide a conductive layer.

3.4.4.1 Objective of SEM

SEM is an outstanding technique for observing the surface of material and provides excruciate details about surface projections. It provides information about

i.   Texture (External Morphology)
ii.   Chemical composition
iii. Orientation
iv.   Crystalline Structure

3.4.4.2 Working Principle

It uses an electron beam to generate the image of a material and the magnifications are obtained by means of electromagnetic fields.

3.4.4.3 Components Of SEM

The components of SEM include

i.   Electron source
ii. Condenser lens
iii. Scan coils
iv. Objective lens
v.   Secondary electron detector

At the top of the column the electrons are generated by the electron source. A beam of electrons is produced. When their thermal energy exceeds the work function of the source, the electrons are emitted. These electrons then get accelerated and are attracted by the anode (positively charged). The diameter of electron beam is adjusted by means of lens. If it is weakened, a broader beam is produced and vice versa. The path of electrons is also controlled by the lens. Electromagnetic lens is utilized owing to the fact that electrons couldn't pass through the glass. Firstly, the electrons meet the

condenser lens. After converging by condenser lens, the electrons are further condensed by the objective lens

Figure 7: Shows the component of SEM [33]

3.4.5. Transmission Electron Microscopy

The Transmission electron microscope uses an electron gun that utilizes electron beam to display he image of specimen. It is having high magnification power approx. 2 million times as compared to light microscope.

3.4.5.1 Working Principle

The working principle is similar to light microscope, except it uses a beam of electron to focus rather than light. As electron exhibit shorter wave length and thus an increase in resolution power occur when electron illuminates, which increases the electron transmission. It has three major working units.

  i. Electron gun.
 ii. Image producing unit.
iii. Image recording unit.

3.4.5.2 Energy dispersive X-ray spectroscopy (EDS)

To analyze the elemental composition of sample, energy dispersive x-ray spectroscopy is a prevailing technique that is used. It majorly works on capacity of x-rays to emit core electrons from an atom. This process is known as Moseley's Law, which shows that as the frequency of light released increases, the atomic number of atoms also increases. When the electron leaves the system, a hole will be created. This hole gets occupied by a higher energy electron, which releases energy as it gets relaxed [128]. The energy released is characteristic to each element in periodic table, which can be used to identify element as well as their proportion. It consists of 3 major parts.

  i. Emitter
 ii. Collector
iii. analyzer

These parts are connected to SEM, or TEM. Combining three pieces gives information about ho may x-rays are released and energy associated with it.

3.5. Electrochemical characterization

3.5.1. Linear sweep voltammetry

A defined potential range is used in the linear sweep voltammetry technique, which is applied in a similar way as potential step measurement. The voltage scanning is performed from lower to upper limit as given below
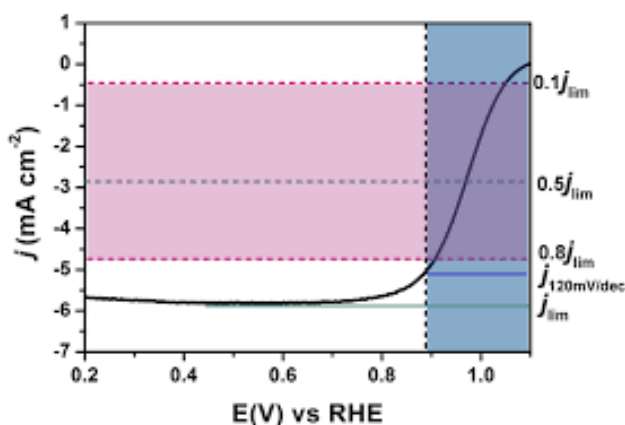

Figure 8: Schematic representation of LSV [23]

The scan rate may be estimated using the line's slope. It depends on time required to sweep the voltage range. The characteristics of LSV curve depends on many factors:

  i.   Reaction rate required to transfer an electron
  ii. The chemical reactivity of species that are electroactive
  iii. The voltage scan rate

The response of current is plotted against voltage.

Tafel slope

To understand the Tafel behaviour, the Tafel slope is used among reactants and electrocatalysts. The Tafel equation can be transformed to log functions, where a low Tafel slope indicates efficient kinetics of electro catalyst which corresponds to smaller overpotential with quick increase in current density. Tafel slope also provides an insight to OER mechanism, pointing out to the rate determining step. the intrinsic rate of electron transfer among electrode and analyte can be directly reflected by exchange current density($j_\circ$). however, the complex OER mechanism and extensive errors associated with exchange current density estimation j0 is rarely used in OER and HER

$$\eta = b. \log \frac{j}{j_\circ}$$

where η = overpotential

b = Tafel slope

j = current density

j. = exchange current density.

Overpotential

For the purpose of formation of reaction intermediates with efficacy overpotential is applied to propel the processes of electron transfer at a desired rate that has been subjected to inactivity because of the high activation energies [26]. Under the conditions that, water is at 25oC and pH = 0 then according to Nernst equation, (Eeq= NHE = RT/NF = $\ln \frac{Ox}{Red}$)

The required potential for electrolization of water will be Eeq = 1.23V vs. NHE.

With the change of pH, the electrode potential changes, which in turn utilizes reversible hydrogen electrode (RHE) as a reference potential at a given temperature of 25oC.

Eeq (RHE) = Eeq (RHE) +0.059 pH =1.23V

The cell potential given as E is

E(RHE)=ETest+Eo+0.059 pH, Where ERHE=converted cell potential

ETest = applied cell potential

$E^°$ = cell potential at standard conditions

For different overpotential values there will be different current values accordingly. The overpotential value was commonly used as criterion at a current density of J=10 mA cm-2 (η10). The smaller the value of η10 more improved will be the electrolytic ability.

Ŋ = E(RHE) - Eeq(RHE)

3.5.2. Cyclic voltammetry (CV)

The voltage is altered between two values at a predetermined rate in cyclic voltammetry testing, which shares many of the same characteristics as LSV and when the voltage hits V2, reverse scanning is conducted, and the voltage is returned to V1. For a reversible single electrode, a cyclic voltammogram is shown. When the voltage increases from V1 toV2 the response is similar to LSV. Reversal of scan shifts the curve from equilibrium position resulting in oxidation. In this case the current flows from electrolyte solution towards the electrode. When electrochemical reaction is performed reversibly the CV has certain characteristics.

   i.   The current peaks separate by voltage of $\Delta E = E$
  ii.   The peak voltage position remains the same as scan rate changes.
 iii.   The ratio of the peak current gives the value of one

$$|ip\ a|\ |ip\ c| = 1$$

iv.   The peak currents are proportional to the square root of the scan rate
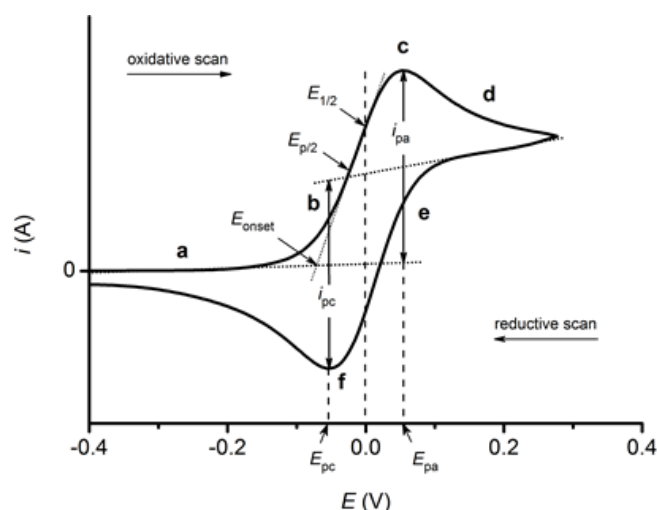

Figure 9: Cyclic voltammetry curve illustration [42]

3.5.3. Electrochemical Impedance Spectroscopy (EIS)

To measure resistance and capacitance properties of catalyst electrochemical impedance spectroscopy is used, when an AC excitation signal is applied at 10 mV. The resistance and capacitance values are calculated by measuring in-phase and out-phase responses of current. It also provides an insight to electrochemical reactions occurring at anode and cathode. Internal resistance is measured in several terms, such as the diffusion transfer resistance, charge transfer resistance and ohmic resistance. The tests are performed in a potentiostat with a frequency range of 100 kHz to 1 MHz and a 10 mV AC amplitude. A frequency response analyzer can be used to record fluctuations in current and voltage response.

Bode or Nyquist plots are used to depict EIS values. The Nyquist plot is drawn by plotting negative imaginary impedance values on x-axis, while real impedance values on y-axis. The Bode plot gives the low and high frequency data. The difference between high frequency and low frequency resistance gives the value Rp. To form an equivalent circuit, the Warburg element is connected in parallel to Rs and Rp to demonstrate diffusion mechanism

3.5.4. Stability test

Electrocatalyst stability is a key activity parameter in OER catalysis that may be assessed in a variety of methods. The cyclic stability depends upon the change in linear sweep voltammetry (LSV) after performing 1000 cycle voltammetry scans. It can also

be depicted by durability test, which is provided by the change in performance at specific current density (chrono-amperometry) or at a specific applied potential (chronopotentiometry) as a function of time. At very long time, it works by performing Galvano static or at potentio-static mode. If the activity of the material does not change after such long-term polarization, it is said to be stable.

Chapter No 4

Results and Discussion

4.1. Characterization of STF based different electrocatalysts

4.1.1. X-ray diffraction analysis

The XRD characterization of the electrocatalysts was examined. In **Figure 10.** we can see the XRD patterns of calcined Sr_2TiFO_6 (STF) and STF/Pr doped electrocatalysts $Sr_2TiFe_{0.9}Pr_{0.1}O6$ (STF$_{0.9}$Pr$_{0.1)}$ and $Sr_{1.9}Pr_{0.1}TiFeO6$ (S$_{1.9}$Pr$_{0.1}$TF). **Figure 10.** shows the peaks at 25.12˚, 32.19˚, 39.7˚, 46.3˚, 57.8˚, 67.8˚, 77.4˚. STF electrocatalyst was recognized as $Sr2TiFeO_6$ (JCPDS # 38-1335) containing that is a cubic structure in the range of pm-3m space group. For STF, the XRD spectra that we obtained are quite close to those that have been published in the literature [115]. Figure 3 depicts the XRD patterns of STF0.9Pr0.1 and S1.9Pr0.1TF. For all Pr doped compositions, there is a slight peak shift that can be seen. Furthermore, as seen in Figure 10, no large peaks have been found this displays a magnified view of the (110) main peak. The peak's intensity, on the other hand, appears to have grown. This suggests that the crystallinity of STF-based doped electrocatalysts has been enhanced, but that the original lattice for S1.9Pr0.1TF has not been distorted and this demonstrates that a certain quantity of Pr is doped into the insufficient A-sites as well as the STF lattice and therefore, removes
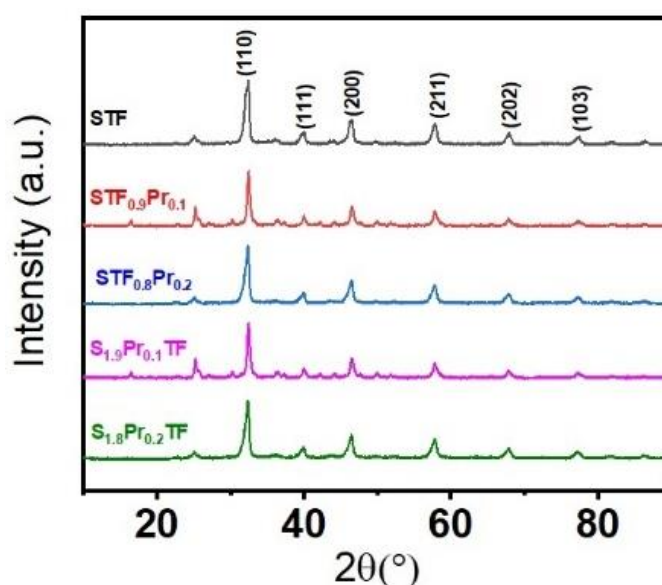

Figure 10: XRD spectrum of STF and doped STF$_{0.9}$Pr$_{0.1}$, STF$_{0.8}$Pr$_{0.2}$, S$_{1.9}$Pr$_{0.1}$TF and S$_{1.8}$Pr$_{0.2}$TF

the defects in the crystal lattice. There are small peaks are observed in B-site doped STF/Pr double perovskites $STF_{0.9}Pr_{0.1}$ due to geometry changing of the lattice. Furthermore, there are no further prominent peaks, showing that the pure phase praseodymium (Pr) layers are efficiently produced on STF particles using the hydrothermal process without any contaminants.

4.1.2. Scanning electron microscopy (SEM)

Figure 11. shows the SEM morphology of the pure STF and Pr/STF doped electrocatalysts at 1μm and 0.5μm field magnifications. The micrographs that are shown in **Fig. 11(a).** indicates the pure STF electrocatalyst, when there is no doping of praseodymium Pr. Pure STF based double perovskites possesses a irregular shaped cluster and a high porous web-like structure, this structure is very supportive for the electrochemical reaction mechanism. Clusters are fine grains of STF aggregates with an average diameter of 35 nm, which contribute to create a porous channel and improve electrolyte mobility. For the transportation of charge, there are interconnecting grain are very helpful. Moreover, in **Fig 11(b)** the structure of STF/Pr doped $STF_{0.9}Pr_{o.1}$ electrocatalyst shows a nano-tube structure and that contain a small hole in tubes which shows a porous structure of electrocatalyst. And in **Fig. 11(c,d)** we can easily observed that there are irregular clusters are present in structure.

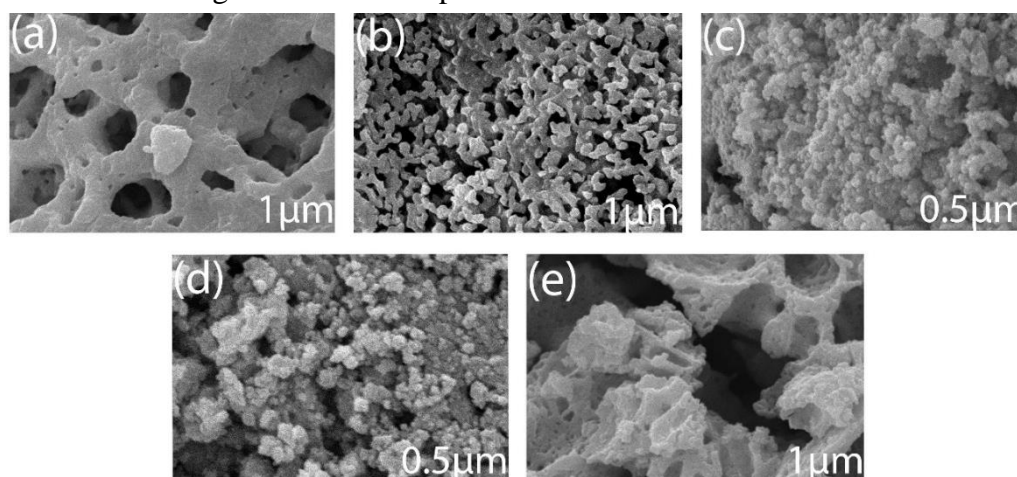*Figure 11: Shows SEM images of pure STF and other doped electrocatalysts*

It shows that there is praseodymium is doped on pure STF electrocatalyst in the form of irregular clusters that increase the surface area that is very helpful in electrochemical reactions. Actually, microporous materials are very supportive for the adsorption and desorption for electrolyte and when compared to microporous, it provides a greater

number of active sites for redox reactions. Micropores, in comparison to macrospores, actively assist electrolyte adsorption and desorption and provide a variety of active sites for redox processes [116].

4.1.3. Fourier Transform Infrared spectroscopy (FTIR)

For further characteristic exploration of pure STF and STF/Pr doped electrocatalysts, Fourier Transform-infrared (FT-IR) procedure was used. Vibration of metal oxide bands in the series between 400-4000cm^{-1} shown in **Fig. 12.** In FTIR, there can be seen broad peaks at 3435 cm^{-1} that is represent the O-H bond stretching vibration, and other small peak can be shown at 1634 cm^{-} that is interlayered of water. Also, FTIR graph that was obtained for the pure STF and doped Pr/STF are presented in Figure 13. And also there is a peak at 856 cm^{-1}, that is a characteristic peak which represent parallels to Sr–O/Ti–O stretching vibrations[117]. And the peaks that is in the region of 1442 to 1456 cm^{-1} relates to the H−O−H stretching vibration of adsorbed water[118]. The additional small peaks are observed for Pr/STF B-site doped material due to change in geometrical structure.
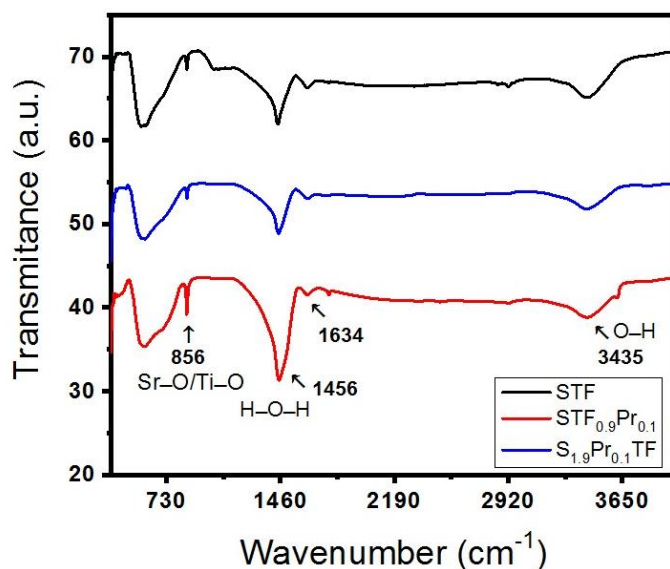
Figure 12: FTIR results for pure STF and doped STF$_{0.9}$Pr$_{0.1}$, STF$_{0.8}$Pr$_{0.2}$, S$_{1.9}$Pr$_{0.1}$TF and S$_{1.8}$Pr$_{0.2}$TF
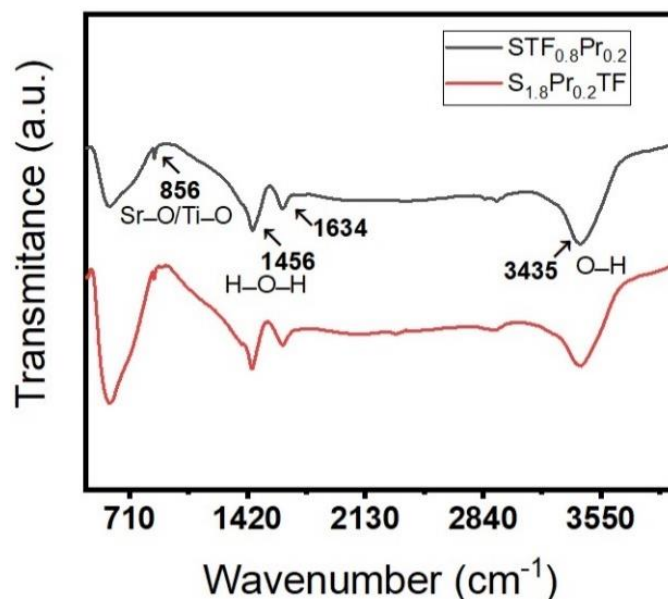
Figure 13: FTIR results for STF$_{0.8}$Pr$_{0.2}$ and S$_{1.8}$Pr$_{0.2}$TF

4.1.4. Transmission Electron Microscope (TEM)

TEM was used to investigate the crystal structure and microstructure differences between the materials shown in **Fig 14**. For the TEM analysis, samples from only one concentration were selected. In this study we have analysis the STF/Pr doped double perovskites electrocatalyst and XRD shows similar pattern for this sample. In this situation, a very porous structure can be seen in the TEM picture of STF/Pr doped electrocatalyst. The size of the grain formed with about 30-35 nm. The rough surface of the STF/Pr doped electrocatalyst composite layers suggests that Pr nanoparticles are efficiently embedded into STF nanosheets, which is consistent with the XRD data. Electrocatalysts with tiny grains and numerous pores may have a large surface area.

Fig. 14(c) shows that the size of lattice fringes having d-spacing is 0.143 nm assure high crystallinity of these nano-structure
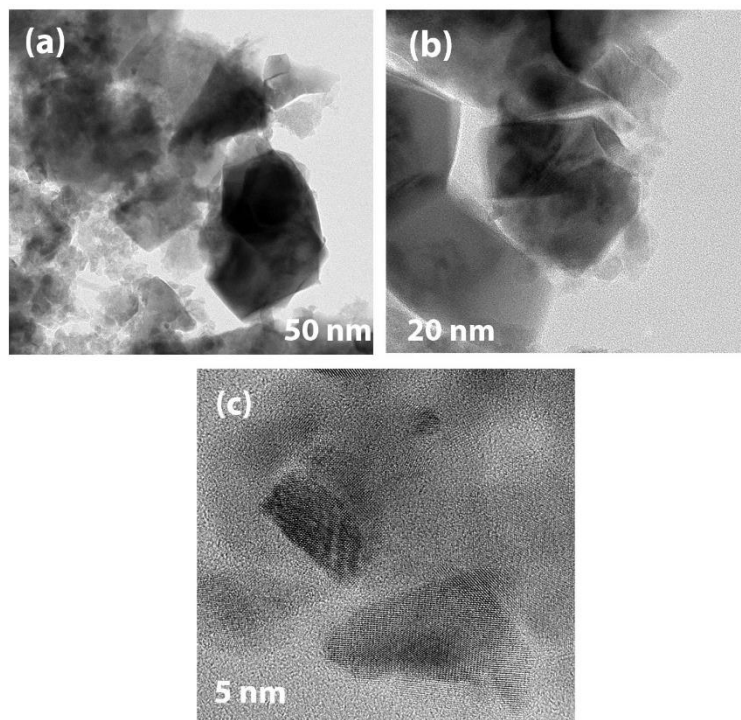
Figure 14: TEM images STF/Pr doped composite at different resolutions, clearly demonstrating Pr layers along with STF nanoparticles

4.1.5. EDS

The analysis of STF based double perovskites electrocatalyst was made to further confirm the formation STF. which validates the presence of Ti, Sr, Fe and O in composite shown in **Fig. 15**. You can see the clear all amounts of Ti, Sr, Fe and O in **Fig. 15(c)**. The multilevel structure of the STF composite was preserved, and various layers of nanoparticles were attached. The elemental mapping of as synthesized material is shown in **Fig. 15(b-f). In Fig. 15(f)** you can see clear doping of praseodymium in nanoparticles of STF. The STF/Pr composite maintained the multilayered structure and has undergone attachment of Pr nanoparticles between STF nanolayers.
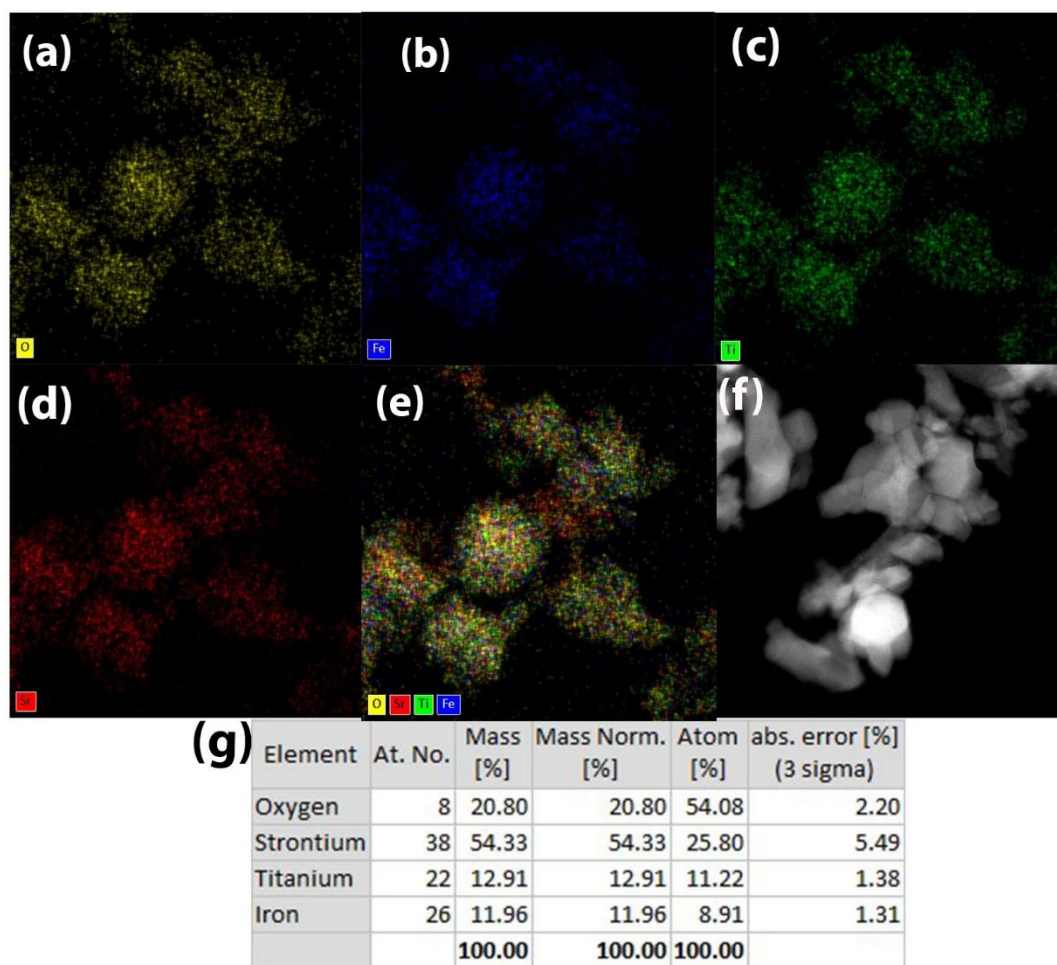
Figure 15: Elemental mapping of STF composite showing presence of Sr, Ti, O, and Fe

Element	At. No.	Mass [%]	Mass Norm. [%]	Atom [%]	abs. error [%] (3 sigma)
Oxygen	8	20.80	20.80	54.08	2.20
Strontium	38	54.33	54.33	25.80	5.49
Titanium	22	12.91	12.91	11.22	1.38
Iron	26	11.96	11.96	8.91	1.31
		100.00	100.00	100.00	

4.2. Electrochemical testing of STF based different electrocatalyst for OER and HER

4.2.1. Linear sweep voltammetry results for OER

To perform electrochemical study, there are 3 electrode assembly that contain of the bare Ni foam, Pt mesh, pure STF and STF/Pr doped electrocatalysts $STF_{0.9}Pr_{0.1}$, $STF_{0.8}Pr_{0.2}$, $S_{0.9}Pr_{0.1}TF$, $S_{0.8}Pr_{0.2}TF$ in one molar KOH solution was used. The LSV polarisation curve was used to estimate the performance of STF's OER. For the study and the impact of heterostructure on Ni foam, we have also synthesized doped STF/Pr electrocatalysts and have tested under alike conditions for the performance of OER. As shown in Figure 16.$Sr_{1.9}Pr_{0.1}TF$ there is a curve for OER we can see the oxidation peak at a potential of 1.38 V which resembles to the Ni oxidation. There is quickly increase of anodic current density of $Sr_{1.9}Pr_{0.1}TF$, when potential is >1.54 V. Linear

sweep voltammetry (LSV) of $Sr_{1.9}Pr_{0.1}TF$ shows excessive difference for OER activities as compare to pure STF and other doped electrocatalysts.
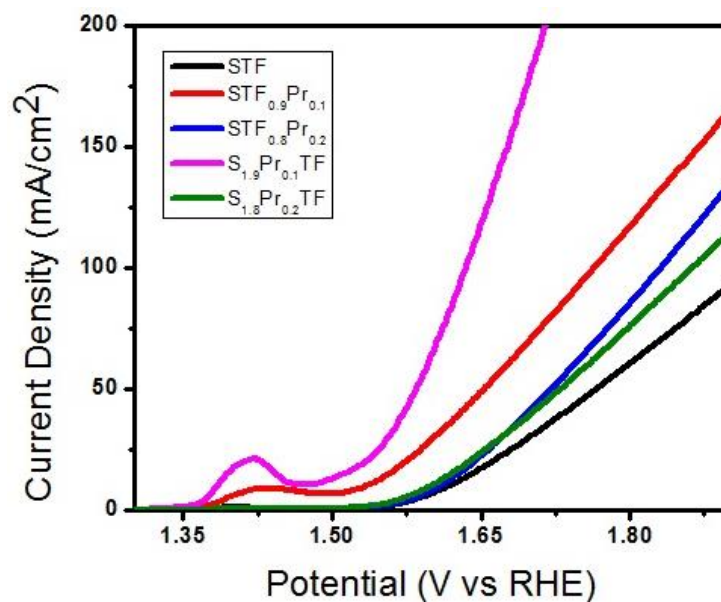
Figure 16 : OER polarization curves for pure STF and doped $STF_{0.9}Pr_{0.1}$, $STF_{0.8}Pr_{0.2}$, $S_{1.9}Pr_{0.1}TF$ and $S_{1.8}Pr_{0.2}TF$
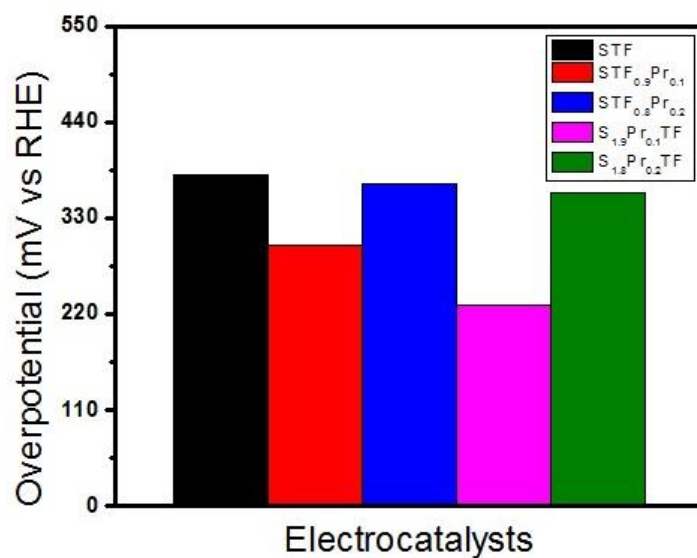
Figure 17: Overpotential results for pure STF and doped $STF_{0.9}Pr_{0.1}$, $STF_{0.8}Pr_{0.2}$, $S_{1.9}Pr_{0.1}TF$ and $S_{1.8}Pr_{0.2}TF$

The doping of praseodymium (Pr) in STF based electrocatalysts perovskites at A-site critically improves the activity of electrocatalyst. There are many vacancies of oxygen are produced by doping of praseodymium Pr in pure STF electrocatalyst. With the help of these vacancies there are more chances to diffuse the oxygen. Another assessment for OER of doped $Sr_{1.9}Pr_{0.1}TF$ by the help of overpotential and anodic current density, which shows that overpotential is required very low for $Sr_{1.9}Pr_{0.1}TF$. That is (230 mV at 10 mA cm-2 current density), that is much less than pure STF and other doped electrocatalysts material. The high electrochemical activity of $S_{1.9}Pr_{0.1}TF$ could be confirmed with the help of low Tafel slope of $S_{1.9}Pr_{0.1}TF$ (136 mV dec-1) as compare to pure STF and other STF/Pr doped electrocatalysts show in **Figure 18**. Thus low vlue of tafel slope for $S_{1.9}Pr_{0.1}TF$ shows that there is higher electrocatalytic activity. Through this, there is a a huge chances of absorbed oxygen spicies and the interaction of catalyst on the cation site.

Figure 18: Corresponding tafel slope for OER of STF, STF$_{0.9}$Pr$_{0.1}$, STF$_{0.8}$Pr$_{0.1}$, S$_{1.9}$Pr$_{0.1}$TF and S$_{1.8}$Pr$_{0.2}$TF

Table 3: Comparison of performance of various perovskites electrocatalysts

Catalyst	Electrolyte	Onset Potential (V) for OER		Ref
STF	1M KOH	1.61		This work
STF$_{0.9}$Pr$_{0.1}$	1M KOH	1.53		This work

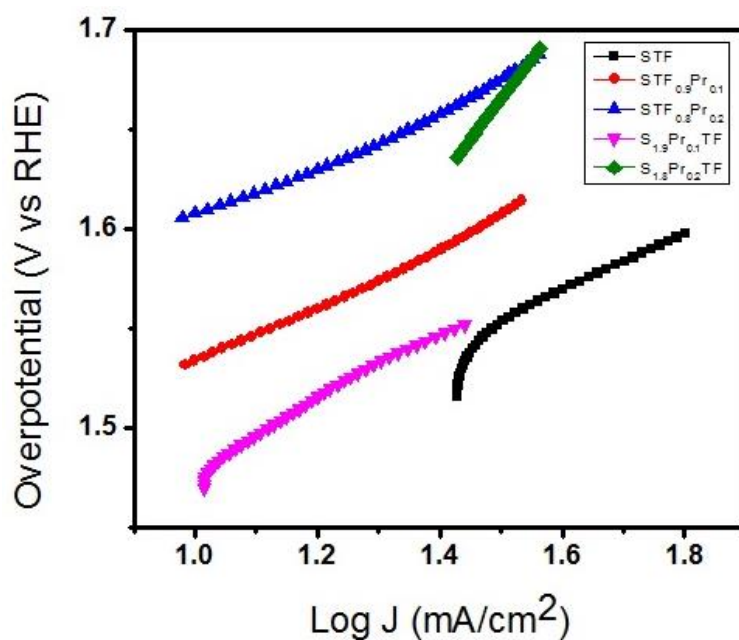|				
STF$_{0.8}$Pr$_{0.2}$	1M KOH	1.60		This work
S$_{0.9}$Pr$_{0.1}$TF	1M KOH	1.46		This work
S$_{0.8}$Pr$_{0.2}$TF	1M KOH	1.59		This work
La $_{1.5}$Sr $_{0.5}$ Ni $_{0.5}$ Mn $_{0.5}$ Ni $_{0.5}$ Ru $_{0.5}$ O $_6$	1M KOH	1.66		[94]
La $_{0.6}$ Sr $_{0.4}$ Co $_{0.2}$ Fe $_{0.8}$ O$_3$	1M KOH	1.6		[94]
24La $_{0.7}$ (Ba $_{0.5}$ Sr $_{0.5}$) $_{0.3}$ Co $_{0.8}$ Fe $_{0.2}$ O$_{3\delta}$	1M KOH	1.60		[97]
Pr Ba $_{0.85}$ Ca $_{0.15}$ Mn FeO $_{5+\delta}$	1M KOH	1.64		[113]
Ba $_{0.5}$ Sr $_{0.5}$ Co $_{0.8}$ Fe $_{0.2}$ O $_{3-\delta}$	1M KOH	1.65		[119]
La $_{0.6}$ Sr $_{0.4}$ Fe $_{0.8}$ Co $_{0.2}$ O3	1M KOH	1.67		[119]

4.2.2. Linear sweep voltammetry for HER

To perform electrochemical study, there are three electrode assembly that contain of the bare Ni foam, Pt mesh, pure STF and STF/Pr doped electrocatalysts STF$_{0.9}$Pr$_{0.1}$, STF$_{0.8}$Pr$_{0.2}$, S$_{0.9}$Pr$_{0.1}$TF, S$_{0.8}$Pr$_{0.2}$TF in one molar KOH solution was used. The performance of OER of STF was estimated through the LSV polarization curve. For the study and the impact of heterostructure on Ni foam, we have also synthesized doped STF/Pr electrocatalysts and have tested under alike conditions for the performance of HER. HER performance shown in **Figure 19**. To estimate the electrocatalytic performance of A-site doped S$_{1.9}$Pr$_{0.1}$TF electrocatalyst, again we
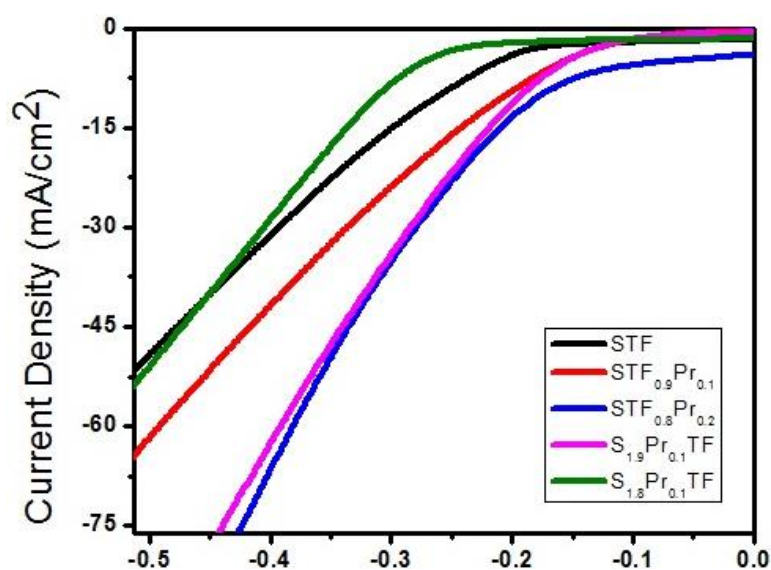
Figure 19: Polarization curve OER for STF, STF$_{0.9}$Pr$_{0.1}$, STF$_{0.8}$Pr$_{0.1}$, S$_{1.9}$Pr$_{0.1}$TF and S$_{1.8}$Pr$_{0.2}$TF 10 mV s-1 in 1 M KOH.

studied the HER performance of synthesized electrocatalyst. The $S_{1.9}Pr_{0.1}TF$, $STF_{0.9}Pr_{0.1}TF$ and $STF_{0.8}Pr_{0.2}$ electrocatalyst shows an excellent activity as HER.

As we know, the most favorable HER catalyst is Pt/C/NF, another assessment for HER of doped $Sr_{1.9}Pr_{0.1}TF$, $STF_{0.9}Pr_{0.1}TF$ and $STF_{0.8}Pr_{0.2}$ by the help of overpotential and anodic current density, which shows that overpotential is required very low for $Sr_{1.9}Pr_{0.1}TF$. That is (180, 190 and 170 mV at 10 mA cm-2 current density), that is much less than pure STF and other doped electrocatalyst material.
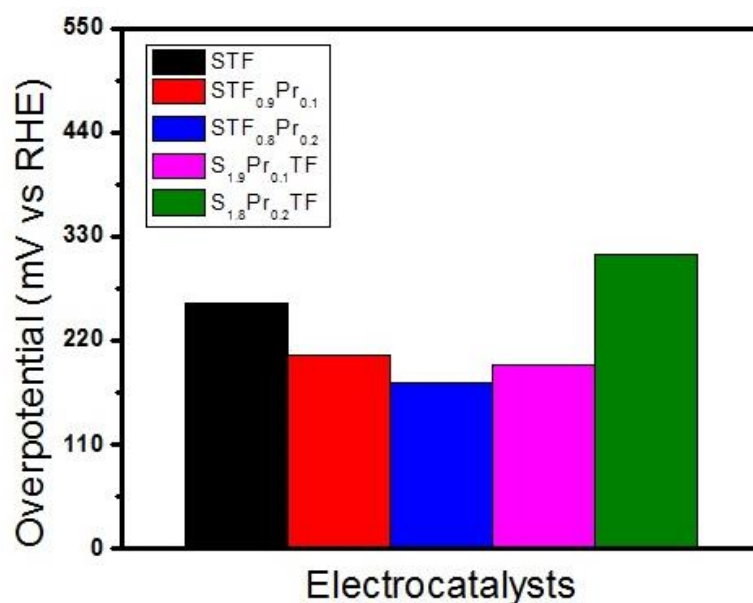
Figure 20: Overpotential required at 10 mA cm^{-2}

The high electrochemical activity can also be confirmed by the low Tafel slope of $S_{1.9}Pr_{0.1}TF$, $STF_{0.9}Pr_{0.1}TF$ and $STF_{0.8}Pr_{0.2}$ (126, 190 and 121) that is low compare to pure STF and other STF/Pr doped electrocatalyst show in **Figure 21**. The low Tafel slope value for $S_{1.9}Pr_{0.1}TF$ shows that there is higher electrocatalytic activity.
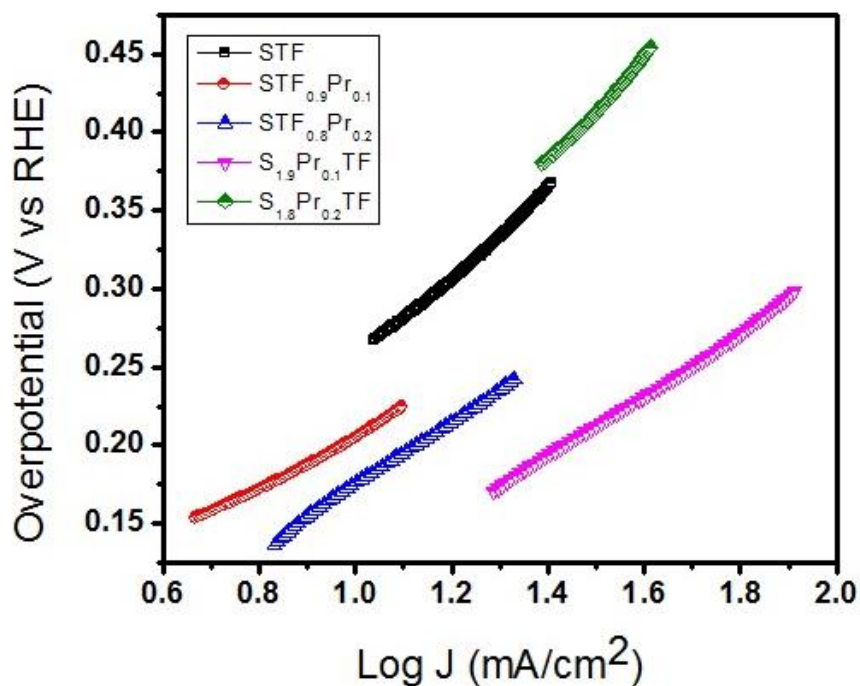
Figure 21: Corresponding Tafel slope for HER of STF, STF$_{0.9}$Pr$_{0.1}$, STF$_{0.8}$Pr$_{0.1}$, S$_{1.9}$Pr$_{0.1}$TF and S$_{1.8}$Pr$_{0.2}$TF

Table 4: Comparison of performance of various perovskites electrocatalysts

Catalyst	Electrolyte	Onset Potential(V) for HER	Ref
STF	1M KOH	0.26	This work
STF$_{0.9}$Pr$_{0.1}$	1M KOH	0.205	This work
STF$_{0.8}$Pr$_{0.2}$	1M KOH	0.176	This work
S$_{0.9}$Pr$_{0.1}$TF	1M KOH	0.194	This work
S$_{0.8}$Pr$_{0.2}$TF	1M KOH	0.311	This work
Ba $_{0.5}$ Sr $_{0.5}$ Co $_{0.8}$ Fe $_{0.2}$ O 3–δ (BSCF)	1M KOH	0.20	[33]
Pr $_{0.5}$ (Ba $_{0.5}$ Sr $_{0.5}$) $_{0.5}$ Co $_{0.8}$ Fe $_{0.2}$ O 3–δ (Pr0.5BSCF)	1M KOH	0.179	[33]

$Sr_{0.95}Co_{0.8}Nb_{0.1}Ni_{0.1}O_{3-\delta}$	1M KOH	0.177	[120]
$La_{0.6}Sr_{0.4}Co_{0.2}Fe_{0.8}O_3$	1M KOH	0.163	[28]
MnCo/NF	1M KOH	0.14	[22]

4.2.3. Cyclic voltammetry

Fig. 22 (a) shows the comparison of cyclic voltammogram of pure STF and STF/Pr doped electrocatalysts STF, $STF_{0.9}Pr_{0.1}$, $STF_{0.8}Pr_{0.1}$, $S_{1.9}Pr_{0.1}TF$, $S_{1.8}Pr_{0.2}TF$ at a scan rate of 10mA/s. All the CV curves represent pair of redox peaks. The highest current density has been observed $S_{1.9}Pr_{0.1}TF$. The comparison of CV curves for STF, $STF_{0.9}Pr_{0.1}$, , $STF_{0.8}Pr_{0.2}$ and $S_{1.8}Pr_{0.2}TF$ shows clear difference in redox peaks as well as current density for the prepared composite. This validates the high capacitance and storage capacity of synthesized composite. **Fig. 22 (b)** shows cyclic voltammetry curves for A-site praseodymium doped electrocatalyst at different scan rates of 10, 20, 30, 40 and 50 mV/s. A pair of distinct redox peaks (corresponding to B-type curves) may be seen in the potential range 1-1.6 (V vs RHE) [147]. Furthermore, the adsorption of OH at the electrode surface may be used to determine the reversibility of the electrode material. When we have to increase the scan rate, shapes of the CV curves remains same and does not change, this result show that there is small resistance, high cyclic stability and the performance of the electrodes are efficient. When we increase the scan rate, their resistance of layer gradually decreases. Besides, the OER activity of nickel foam is very low, so that the contribution of nickel foam in
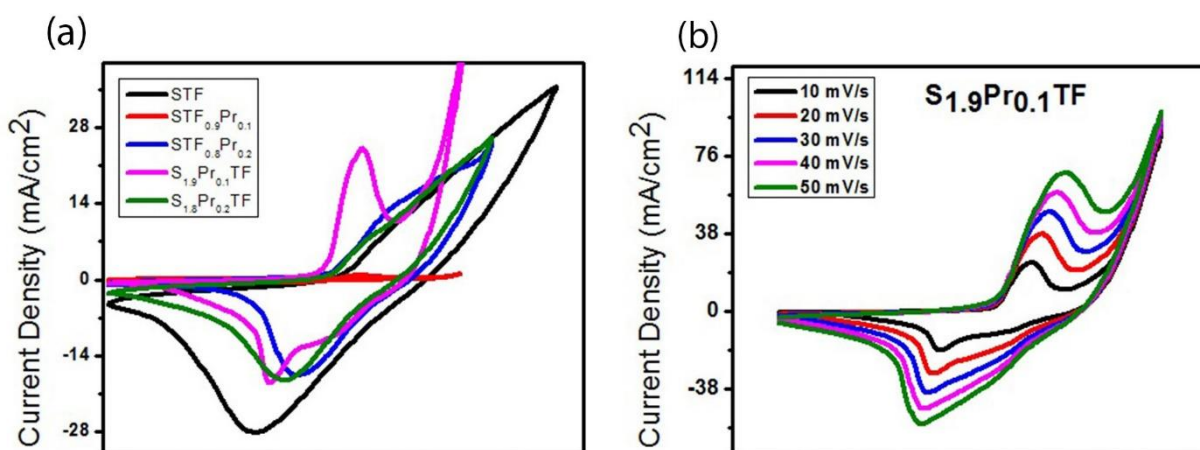
Figure 22: (a) CV curves for STF, $STF_{0.9}Pr_{0.1}$, $STF_{0.8}Pr_{0.2}$, $S_{1.9}Pr_{0.1}TF$ and $S_{1.8}Pr_{0.2}TF$ at scan rate of 10mV/s. (b) CV curves for $S_{1.9}Pr_{0.1}TF$ at scan rate of 10 ,20, 30, 40 and 50 mV/s

OER activity is minimum, it only functions to provide a conductive support to catalyst material[121], [122].

The CV curves for STF, $STF_{0.9}Pr_{0.1}$, $STF_{0.9}Pr_{0.1}$, $STF_{0.8}Pr_{0.2}$, $S_{1.8}Pr_{0.2}TF$ are shown in **Figure 23 (a-d)**. The cyclic voltammogram are obtained at a scan rate of 10 to 50 mVs^{-1}. The range of potential in between 0-1.6 V shows the certain types of redox peaks pairs (corresponding to B-type curves) [123]. shapes of the CV curves remain same and does not change, this result show that there is small resistance, high cyclic stability and the performance of the electrodes are efficient. When the scan rate is increasing, resistance of diffusion layer reduces, so reaching the current densities at higher point.
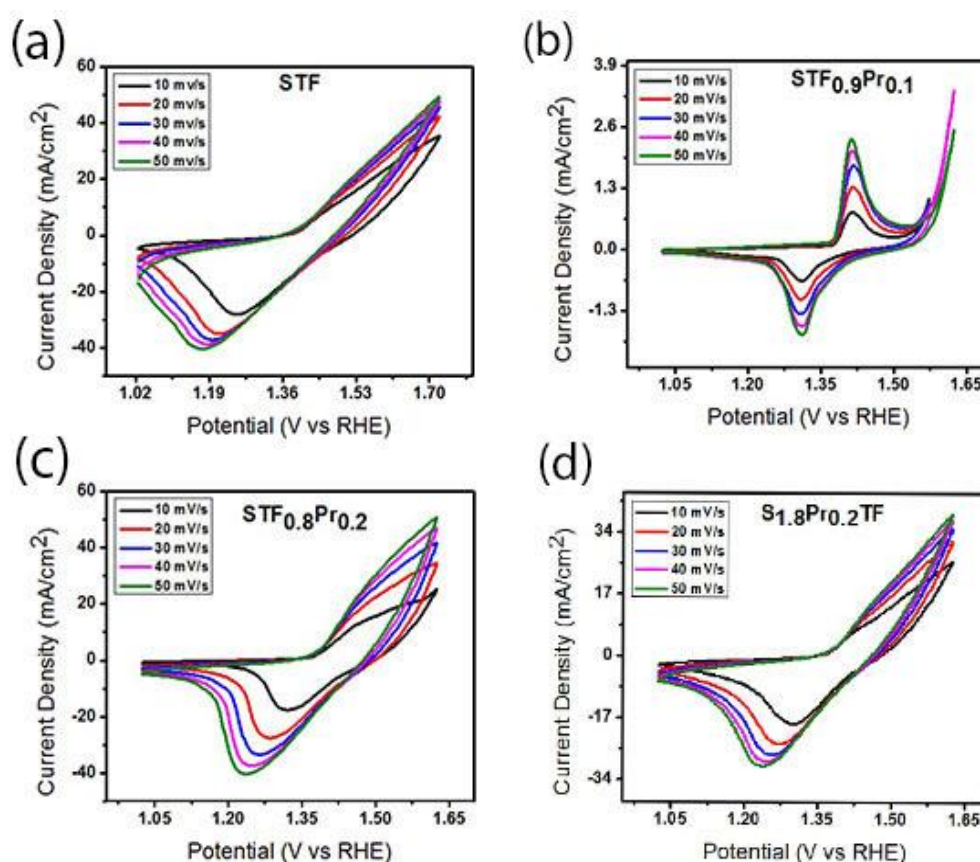
Figure 23: (a-d) CV curves at scan rate 10, 20, 30, 40, 50 mV s -1 for STF, $STF_{0.9}Pr_{0.1}$, $STF_{0.8}Pr_{0.2}$ and $S_{1.8}Pr_{0.2}TF$.

4.2.4. Electrochemical impedance spectroscopy

Furthermore, I have used the impedance spectroscopy for further study the kinetics of as synthesized electrocatalyst (Fig. 42(a)). I have performed the test, and frequency range was 2MHz – 0.1Hz and solution was 1 M KOH. Alongside, the Nyquist plot that is shown in **figure 24.** also represent a semicircle that is related to the resistance of polarization. This polarization resistance is the result of faradic reaction that are

performing at the surface of electrodes. The reduced charge transfer resistance (Rct) has been observed for $S_{1.9}Pr_{0.1}TF$ which is shown by a small diameter of semicircle indicating the proficient charge transferability[124] [125]
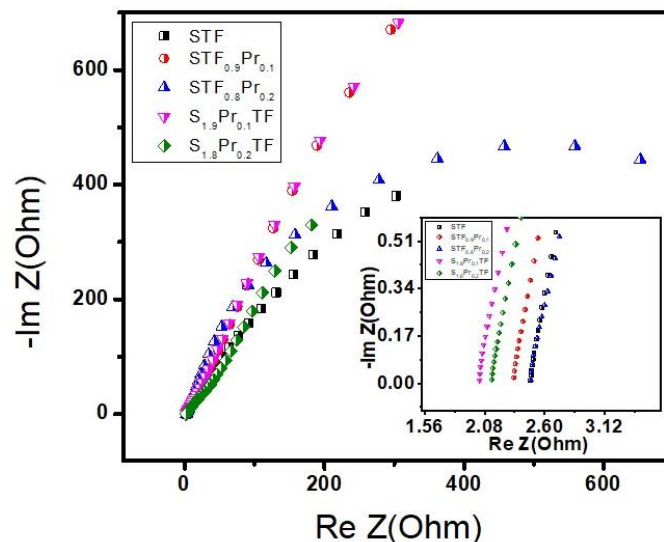
Figure 24: The Nyquist plot at frequency 2Mhz-0.1Hz for STF, STF$_{0.9}$Pr$_{0.1}$, STF$_{0.8}$Pr$_{0.2}$, S$_{1.9}$Pr$_{0.1}$TF and S$_{1.8}$Pr$_{0.2}$TF.

4.2.5. Stability Test

In further, I have been study for the STF/Pr doped $S_{1.9}Pr_{0.1}TF$ electrocatalyst was observed for the test of stability at 10 mA for 24 hrs. **Figure 25 (a))**. Shows that there is a potential from the chronopotentiometry was stable behavior of nanocomposites, that was achieved by its structural characteristics. There is a low ion diffusion that was derived through area of interfacial between electrolyte and electrodes that is favorable quick ion penetration across the widely exposed active sites. This is due to activation of material synthesized during chronopotentiometry test. The potential achieved the constant value with potential change of only 0.03 V, which shows a very stable catalyst with high efficiency. The stability of $S_{1.9}Pr_{0.1}TF$ was also confirmed by undergoing linear sweep voltammetry analysis after performing 1000 cycles, shown in **Fig. 25(b).** The LSV results were found similar after 1000 cycles to the initial value of LSV. These results make $S_{1.9}Pr_{0.1}TF$ catalyst quite stable for practical application.
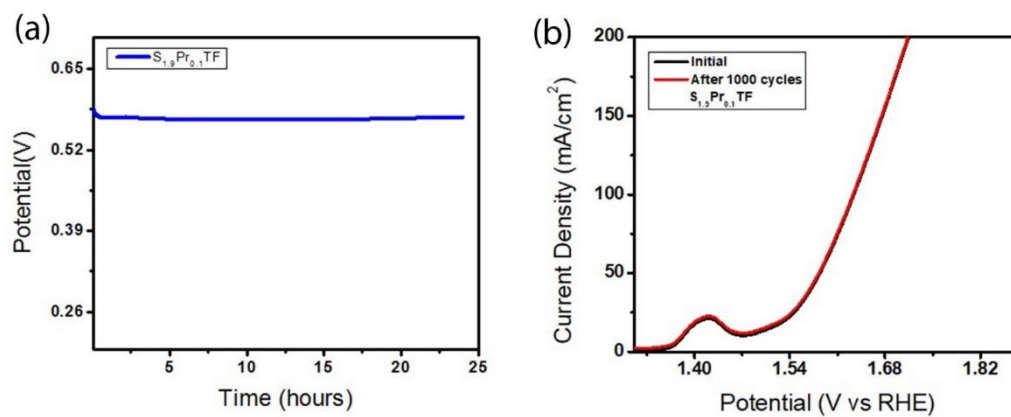
Figure 25: (a) Chronopotentiometry curve for $S_{1.9}Pr_{0.1}TF$ for 24 hrs. (b) Stability test for $S_{1.9}Pr_{0.1}TF$ showing linear sweep voltammetry result after 1000 cycles.

Conclusions

This report gives the study about the development about double perovskite oxides electrocatalysts for OER and HER as water splitting. To find the low cost, non-precious, stable and efficient electrocatalysts for water splitting reactions. Thus, to overcome the cost we have developed the STF based double perovskites that were more favorable for efficient catalytic properties. Double perovskites have been study deeply regarding to their flexible ionic crystal structure as well as ability of substitution in A/B site cation. We have determined the effects of A-site doping as well as B-site by doping the small amount of rare earth metal oxide that helps to enhance the catalytic activity.

In this regard, we have presented a highly efficient and active STF based double perovskites towards electrolysis of water for the production of hydrogen. In this study, pure (Sr_2TiFO_6) STF based double perovskites and STF/Pr doped electrocatalysts by doping the rare earth metal praseodymium Pr at A-site and B-site were made by sol-gel method. The Sr_2TiFO_6 (STF) based electrocatalysts was characterized by XRD, SEM and FTIR and electrochemical performance was analyzed by using 3-electrode testing in alkaline media. The results of STF Sr_2TiFO_6 (STF) based double perovskites towards OER (Oxygen Evolution Reaction) and HER (Hydrogen Evolution Reaction) was very remarkable. The OER results for $S_{1.9}Pr_{0.1}TF$ showed overpotential of 230 at current density of 10mA/cm^2 and Tafel slope was 139 mV dec^{-1}. For HER, there was overpotential of 194mV at current density of 10mA/cm^2 and Tafel slope was 126 mV dec^{-1}. Moreover, it exhibits notable results of durability for 24 hours. With the help of Sr_2TiFO_6 (STF) based double perovskites electrocatalysts, we can develop more efficient process and enhance the activity towards water splitting reactions.

Although, there is a lot of research have been done in the applications of double perovskites as electrocatalysts for water splitting. But there is still gap is present for further development in the field of water splitting, especially in demand of hydrogen evolution reaction HER. Since, both OER and HER reactions are different in nature, there will be a still challenge for synthesize such bifunctional electrocatalyst for water splitting. However, it might be possible to achieve the desired activities of the perovskite based bifunctional catalysts by further studies designed to undertake the challenge.

Future Recommendations

- Methods for the synthesis of double perovskites needs to be optimized
- By combining the reaction mechanisms and optimization of the catalyst design, it could be possible that we may quickly develop the active and more efficient double perovskite as HER electrocatalysts.
- Similarly, for the industrial application, owing to the lower value of HER activity of the perovskite catalyst, there might be possibility to explore the application of hybrid catalysts i.e. separate catalyst for both OER and HER.
- Regeneration of catalyst is also an effective area to work in this field.

References

[1]   X. Li *et al.*, "Water splitting: from electrode to green energy system," vol. 12, no. 1, pp. 1-29, 2020.

[2]   R. Khan *et al.*, "Role of perovskites as a bi-functional catalyst for electrochemical water splitting: a review," vol. 44, no. 12, pp. 9714-9747, 2020.

[3]   J. A. J. S. Turner, "Sustainable hydrogen production," vol. 305, no. 5686, pp. 972-974, 2004.

[4]   T. R. Cook, D. K. Dogutan, S. Y. Reece, Y. Surendranath, T. S. Teets, and D. G. J. C. r. Nocera, "Solar energy supply and storage for the legacy and nonlegacy worlds," vol. 110, no. 11, pp. 6474-6502, 2010.

[5]   N. S. Lewis and D. G. J. P. o. t. N. A. o. S. Nocera, "Powering the planet: Chemical challenges in solar energy utilization," vol. 103, no. 43, pp. 15729-15735, 2006.

[6]   Z. W. Seh, J. Kibsgaard, C. F. Dickens, I. Chorkendorff, J. K. Nørskov, and T. F. J. S. Jaramillo, "Combining theory and experiment in electrocatalysis: Insights into materials design," vol. 355, no. 6321, 2017.

[7]   R. Selin, "The outlook for energy: a view to 2040," 2013.

[8]   J. M. Campos-Martin, G. Blanco-Brieva, and J. L. J. A. C. I. E. Fierro, "Hydrogen peroxide synthesis: an outlook beyond the anthraquinone process," vol. 45, no. 42, pp. 6962-6984, 2006.

[9]   H. Ding, C. Luo, X. Li, D. Cao, Q. Shen, and L. J. F. Zhang, "Development of BaSrCo-based perovskite for chemical-looping steam methane reforming: A study on synergistic effects of A-site elements and CeO2 support," vol. 253, pp. 311-319, 2019.

[10]   Y. Xiao, H.-X. Huang, D.-M. Liang, and C. J. C. P. L. Wang, "Electrocatalytic properties and modification of La0. 6Ca0. 4Co1− xMnxO3 (x= 0–0.9) perovskite-type oxides," vol. 738, p. 136846, 2020.

[11]   F. Song *et al.*, "Transition metal oxides as electrocatalysts for the oxygen evolution reaction in alkaline solutions: an application-inspired renaissance," vol. 140, no. 25, pp. 7748-7759, 2018.

[12]   J. Wang, W. Cui, Q. Liu, Z. Xing, A. M. Asiri, and X. J. A. m. Sun, "Recent progress in cobalt-based heterogeneous catalysts for electrochemical water splitting," vol. 28, no. 2, pp. 215-230, 2016.

[13]   J. Yu, Q. Wang, D. O'Hare, and L. J. C. S. R. Sun, "Preparation of two dimensional layered double hydroxide nanosheets and their applications," vol. 46, no. 19, pp. 5950-5974, 2017.

[14]   L. Lv, Z. Yang, K. Chen, C. Wang, and Y. J. A. E. M. Xiong, "2D layered double hydroxides for oxygen evolution reaction: from fundamental design to application," vol. 9, no. 17, p. 1803358, 2019.

[15]   S. Gupta, W. Kellogg, H. Xu, X. Liu, J. Cho, and G. J. C. A. A. J. Wu, "Bifunctional perovskite oxide catalysts for oxygen reduction and evolution in alkaline media," vol. 11, no. 1, pp. 10-21, 2016.

[16]   M. Gong and H. J. N. R. Dai, "A mini review of NiFe-based materials as highly active oxygen evolution reaction electrocatalysts," vol. 8, no. 1, pp. 23-39, 2015.

[17]   N.-T. Suen, S.-F. Hung, Q. Quan, N. Zhang, Y.-J. Xu, and H. M. J. C. S. R. Chen, "Electrocatalysis for the oxygen evolution reaction: recent development and future perspectives," vol. 46, no. 2, pp. 337-365, 2017.

[18]   H. Osgood, S. V. Devaguptapu, H. Xu, J. Cho, and G. J. N. T. Wu, "Transition metal (Fe, Co, Ni, and Mn) oxides for oxygen reduction and evolution bifunctional catalysts in alkaline media," vol. 11, no. 5, pp. 601-625, 2016.

[19]   M. Tahir *et al.*, "Electrocatalytic oxygen evolution reaction for energy conversion and storage: a comprehensive review," vol. 37, pp. 136-157, 2017.

[20]   T. Liu *et al.*, "Enhanced electrocatalysis for energy-efficient hydrogen production over CoP catalyst with nonelectroactive Zn as a promoter," vol. 7, no. 15, p. 1700020, 2017.

[21]   C. Xiong *et al.*, "Nitrogen-doped carbon nanotubes as catalysts for oxygen reduction reaction," vol. 215, pp. 216-220, 2012.

[22]   J. Bao *et al.*, "Two-dimensional Mn-Co LDH/Graphene composite towards high-performance water splitting," vol. 8, no. 9, p. 350, 2018.

[23]   Y. Wang, D. Yan, S. El Hankari, Y. Zou, and S. J. A. S. Wang, "Recent progress on layered double hydroxides and their derivatives for electrocatalytic water splitting," vol. 5, no. 8, p. 1800064, 2018.

[24]   S. Liu *et al.*, "The synergistic effect of Ni promoter on Mo-S/CNT catalyst towards hydrodesulfurization and hydrogen evolution reactions," vol. 232, pp. 36-44, 2018.

[25]   S. Hussain *et al.*, "WS (1− x) Sex nanoparticles decorated three-dimensional graphene on nickel foam: A robust and highly efficient electrocatalyst for the hydrogen evolution reaction," vol. 8, no. 11, p. 929, 2018.

[26]   X. Zhang, Q. Zhang, Y. Sun, and J. J. F. Guo, "Hybrid catalyst of MoS2-CoMo2S4 on graphene for robust electrochemical hydrogen evolution," vol. 184, pp. 559-564, 2016.

[27]   Y. Hou *et al.*, "Vertically oriented cobalt selenide/NiFe layered-double-hydroxide nanosheets supported on exfoliated graphene foil: an efficient 3D electrode for overall water splitting," vol. 9, no. 2, pp. 478-483, 2016.

[28]   X. Zou and Y. J. C. S. R. Zhang, "Noble metal-free hydrogen evolution catalysts for water splitting," vol. 44, no. 15, pp. 5148-5180, 2015.

[29]   A. J. H. o. f. c. Lasia, "Hydrogen evolution reaction," vol. 815, 2010.

[30]   O. Diaz-Morales, F. Calle-Vallejo, C. de Munck, and M. T. J. C. S. Koper, "Electrochemical water splitting by gold: evidence for an oxide decomposition mechanism," vol. 4, no. 6, pp. 2334-2343, 2013.

[31]   Z.-L. Wang, D. Xu, J.-J. Xu, and X.-B. J. C. S. R. Zhang, "Oxygen electrocatalysts in metal–air batteries: from aqueous to nonaqueous electrolytes," vol. 43, no. 22, pp. 7746-7786, 2014.

[32]   J. Bockris, I. Ammar, and A. J. T. J. o. P. C. Huq, "The mechanism of the hydrogen evolution reaction on platinum, silver and tungsten surfaces in acid solutions," vol. 61, no. 7, pp. 879-886, 1957.

[33]   X. Xu *et al.*, "A perovskite electrocatalyst for efficient hydrogen evolution reaction," vol. 28, no. 30, pp. 6442-6448, 2016.

[34]   J. D. Benck, T. R. Hellstern, J. Kibsgaard, P. Chakthranont, and T. F. J. A. C. Jaramillo, "Catalyzing the hydrogen evolution reaction (HER) with molybdenum sulfide nanomaterials," vol. 4, no. 11, pp. 3957-3971, 2014.

[35]   R. J. T. o. t. F. S. Parsons, "The rate of electrolytic hydrogen evolution and the heat of adsorption of hydrogen," vol. 54, pp. 1053-1063, 1958.

[36]   S. J. J. o. E. C. Trasatti and I. Electrochemistry, "Electrocatalysis by oxides—attempt at a unifying approach," vol. 111, no. 1, pp. 125-131, 1980.

[37]   S. J. E. A. Trasatti, "Electrocatalysis in the anodic evolution of oxygen and chlorine," vol. 29, no. 11, pp. 1503-1512, 1984.

[38]   B. JO'M, T. Otagawa, V. J. J. o. E. C. Young, and I. Electrochemistry, "Solid state surface studies of the electrocatalysis of oxygen evolution on perovskites," vol. 150, no. 1-2, pp. 633-643, 1983.

[39]   J. O. M. Bockris and T. J. T. J. o. P. C. Otagawa, "Mechanism of oxygen evolution on perovskites," vol. 87, no. 15, pp. 2960-2971, 2002.

[40]   I. C. Man *et al.*, "Universality in oxygen evolution electrocatalysis on oxide surfaces," vol. 3, no. 7, pp. 1159-1165, 2011.

[41]   D. A. Kuznetsov *et al.*, "Tuning redox transitions via inductive effect in metal oxides and complexes, and implications in oxygen electrocatalysis," vol. 2, no. 2, pp. 225-244, 2018.

[42]   J. Suntivich, H. A. Gasteiger, N. Yabuuchi, H. Nakanishi, J. B. Goodenough, and Y. J. N. c. Shao-Horn, "Design principles for oxygen-reduction activity on perovskite oxide catalysts for fuel cells and metal–air batteries," vol. 3, no. 7, pp. 546-550, 2011.

[43]   J. Suntivich, K. J. May, H. A. Gasteiger, J. B. Goodenough, and Y. J. S. Shao-Horn, "A perovskite oxide optimized for oxygen evolution catalysis from molecular orbital principles," vol. 334, no. 6061, pp. 1383-1385, 2011.

[44]   R. F. J. J. o. T. E. S. Scarr, "The mechanism of oxygen evolution on nickel, platinum, and other metals and alloys," vol. 116, no. 11, p. 1526, 1969.

[45]   S. Mitrovski and D. M. DRAŽIC, "Oxygen evolution at La Ba, CoO3 perovskite-type electrodes," 1998.

[46]   G. Beni, L. Schiavone, J. Shay, W. Dautremont-Smith, and B. J. N. Schneider, "Electrocatalytic oxygen evolution on reactively sputtered electrochromic iridium oxide films," vol. 282, no. 5736, pp. 281-283, 1979.

[47]   T. Ioroi, N. Kitazawa, K. Yasuda, Y. Yamamoto, and H. J. J. o. t. E. S. Takenaka, "Iridium oxide/platinum electrocatalysts for unitized regenerative polymer electrolyte fuel cells," vol. 147, no. 6, p. 2018, 2000.

[48]   L. Da Silva, V. Alves, M. Da Silva, S. Trasatti, and J. J. E. A. Boodts, "Oxygen evolution in acid solution on IrO2+ TiO2 ceramic films. A study by impedance, voltammetry and SEM," vol. 42, no. 2, pp. 271-281, 1997.

[49]   A. Marshall, B. Børresen, G. Hagen, M. Tsypkin, and R. J. E. Tunold, "Hydrogen production by advanced proton exchange membrane (PEM) water

electrolysers—Reduced energy consumption by improved electrocatalysis," vol. 32, no. 4, pp. 431-436, 2007.

[50]   A. Marshall, B. Børresen, G. Hagen, M. Tsypkin, and R. J. E. A. Tunold, "Electrochemical characterisation of IrxSn1− xO2 powders as oxygen evolution electrocatalysts," vol. 51, no. 15, pp. 3161-3167, 2006.

[51]   F. Gutmann and O. J. Murphy, "The electrochemical splitting of water," in *Modern aspects of electrochemistry*: Springer, 1983, pp. 1-82.

[52]   R. Yeo, J. Orehotsky, W. Visscher, and S. J. J. o. t. E. S. Srinivasan, "Ruthenium-Based Mixed Oxides as Electrocatalysts for Oxygen Evolution in Acid Electrolytes," vol. 128, no. 9, p. 1900, 1981.

[53]   K. Izumiya, E. Akiyama, H. Habazaki, N. Kumagai, A. Kawashima, and K. J. E. A. Hashimoto, "Anodically deposited manganese oxide and manganese–tungsten oxide electrodes for oxygen evolution from seawater," vol. 43, no. 21-22, pp. 3303-3312, 1998.

[54]   A. Tseung and S. J. E. A. Jasem, "Oxygen evolution on semiconducting oxides," vol. 22, no. 1, pp. 31-34, 1977.

[55]   Y. Matsumoto and E. J. E. A. Sato, "Oxygen evolution on La1− xSrxMnO3 electrodes in alkaline solutions," vol. 24, no. 4, pp. 421-423, 1979.

[56]   Y. Matsumoto, H. Manabe, and E. J. J. o. T. E. S. Sato, "Oxygen Evolution on La1− x Sr x CoO3 Electrodes in Alkaline Solutions," vol. 127, no. 4, p. 811, 1980.

[57]   A. Kobussen, F. Van Buren, T. Van den Belt, and H. J. J. o. E. C. Van Wees, "Oxygen evolution on LaCoO3-type electrodes," vol. 96, no. 1, pp. 123-125, 1979.

[58]   A. Mai, V. A. Haanappel, S. Uhlenbruck, F. Tietz, and D. J. S. S. I. Stöver, "Ferrite-based perovskites as cathode materials for anode-supported solid oxide fuel cells: Part I. Variation of composition," vol. 176, no. 15-16, pp. 1341-1350, 2005.

[59]   C. Jin, X. Cao, L. Zhang, C. Zhang, and R. J. J. o. p. s. Yang, "Preparation and electrochemical properties of urchin-like La0. 8Sr0. 2MnO3 perovskite oxide as a bifunctional catalyst for oxygen reduction and oxygen evolution reaction," vol. 241, pp. 225-230, 2013.

[60]   J. O. M. Bockris and T. J. J. o. T. E. S. Otagawa, "The electrocatalysis of oxygen evolution on perovskites," vol. 131, no. 2, p. 290, 1984.

[61]   W. Zhou and J. J. T. j. o. p. c. l. Sunarso, "Enhancing bi-functional electrocatalytic activity of perovskite by temperature shock: A case study of LaNiO3− δ," vol. 4, no. 17, pp. 2982-2988, 2013.

[62]   W. T. Hong *et al.*, "Toward the rational design of non-precious transition metal oxides for oxygen electrocatalysis," vol. 8, no. 5, pp. 1404-1427, 2015.

[63]   O. Gwon, "Systematic Study on Electrocatalytic Properties of Perovskite Oxides for Energy Conversion and Storage Systems," 2019.

[64]   L. C. Seitz, *Developing Enhanced Mixed Metal Oxide Catalysts for Electrocatalytic Water Oxidation Using Insights from X-Ray Absorption Spectroscopy*. Stanford University, 2015.

[65]   D. U. Lee, P. Xu, Z. P. Cano, A. G. Kashkooli, M. G. Park, and Z. J. J. o. M. C. A. Chen, "Recent progress and perspectives on bi-functional oxygen electrocatalysts for advanced rechargeable metal–air batteries," vol. 4, no. 19, pp. 7107-7134, 2016.

[66]   L. M. J. I. Q. Valencia Osorio, "Catalizadores bifuncionales basados en estructuras tipo perovskita para baterías zinc-aire."

[67]   J. Suntivich and K. J. S. May, "H. a. Gasteiger, JB Goodenough and Y. Shao-horn," vol. 334, no. 6061, pp. 1383-1385, 2011.

[68]   J. Serra, V. Vert, M. Betz, V. Haanappel, W. Meulenberg, and F. J. J. o. t. E. S. Tietz, "Screening of A-Substitution in the System A0. 68Sr0. 3Fe0. 8Co0. 2O3− δ for SOFC Cathodes," vol. 155, no. 2, p. B207, 2007.

[69]   N. S. Arul and V. D. Nithya, *Revolution of Perovskite*. Springer, 2020.

[70]   A. Hossain, P. Bandyopadhyay, S. J. J. o. A. Roy, and Compounds, "An overview of double perovskites A2B′ B ″O6 with small ions at A site: Synthesis, structure and magnetic properties," vol. 740, pp. 414-427, 2018.

[71]   N. F. Atta, A. Galal, and S. M. J. I. J. E. S. Ali, "The catalytic activity of ruthenates ARuO3 (A= Ca, Sr or Ba) for the hydrogen evolution reaction in acidic medium," vol. 7, pp. 725-746, 2012.

[72]   S. She *et al.*, "Systematic Study of Oxygen Evolution Activity and Stability on La1–x Sr x FeO3− δ Perovskite Electrocatalysts in Alkaline Media," vol. 10, no. 14, pp. 11715-11721, 2018.

[73]   N.-I. Kim *et al.*, "B-site doping effects of NdBa 0.75 Ca 0.25 Co 2 O 5+ δ double perovskite catalysts for oxygen evolution and reduction reactions," vol. 6, no. 36, pp. 17807-17818, 2018.

[74] S. Tiwari, S. Singh, and R. J. J. o. t. E. S. Singh, "Effects of Ni, Fe, Cu, and Cr substitutions for Co in La0. 8Sr0. 2CoO3 on electrocatalytic properties for oxygen evolution," vol. 143, no. 5, p. 1505, 1996.

[75] K. J. May *et al.*, "Influence of oxygen evolution during water oxidation on the surface of perovskite oxide catalysts," vol. 3, no. 22, pp. 3264-3270, 2012.

[76] Y.-M. Chang, Y.-F. Chang, P.-W. Wu, C.-Y. Wu, and P. J. J. o. t. E. S. Lin, "Synthesis and characterization of La0. 6Ca0. 4Co0. 8Ru0. 2O3 for oxygen reduction reaction in an alkaline electrolyte," vol. 157, no. 6, p. B900, 2010.

[77] K. Sivula and R. J. N. R. M. Van De Krol, "Semiconducting materials for photoelectrochemical energy conversion," vol. 1, no. 2, pp. 1-16, 2016.

[78] I. Roger, M. A. Shipman, and M. D. J. N. R. C. Symes, "Earth-abundant catalysts for electrochemical and photoelectrochemical water splitting," vol. 1, no. 1, pp. 1-13, 2017.

[79] D. Voiry, H. S. Shin, K. P. Loh, and M. J. N. R. C. Chhowalla, "Low-dimensional catalysts for hydrogen evolution and CO 2 reduction," vol. 2, no. 1, pp. 1-17, 2018.

[80] P. G. Bruce, S. A. Freunberger, L. J. Hardwick, and J.-M. J. N. m. Tarascon, "Li–O 2 and Li–S batteries with high energy storage," vol. 11, no. 1, pp. 19-29, 2012.

[81] J.-h. Myung, D. Neagu, D. N. Miller, and J. T. J. N. Irvine, "Switching on electrocatalytic activity in solid oxide cells," vol. 537, no. 7621, pp. 528-531, 2016.

[82] L. Lu, J. S. Guest, C. A. Peters, X. Zhu, G. H. Rau, and Z. J. J. N. S. Ren, "Wastewater treatment for carbon capture and utilization," vol. 1, no. 12, pp. 750-758, 2018.

[83] W.-D. Oh, Z. Dong, and T.-T. J. A. C. B. E. Lim, "Generation of sulfate radical through heterogeneous catalysis for organic contaminants removal: current development, challenges and prospects," vol. 194, pp. 169-201, 2016.

[84] J. Hwang, R. R. Rao, L. Giordano, Y. Katayama, Y. Yu, and Y. J. S. Shao-Horn, "Perovskites in catalysis and electrocatalysis," vol. 358, no. 6364, pp. 751-756, 2017.

[85] W. Wang, M. O. Tadé, and Z. J. C. S. R. Shao, "Research progress of perovskite materials in photocatalysis-and photovoltaics-related energy

conversion and environmental treatment," vol. 44, no. 15, pp. 5371-5408, 2015.

[86]   C. J. Howard, B. J. Kennedy, and P. M. J. A. C. S. B. S. S. Woodward, "Ordered double perovskites–a group-theoretical analysis," vol. 59, no. 4, pp. 463-471, 2003.

[87]   G. King and P. M. J. J. o. M. C. Woodward, "Cation ordering in perovskites," vol. 20, no. 28, pp. 5785-5796, 2010.

[88]   S. Vasala and M. J. P. i. s. s. c. Karppinen, "A2B′ B ″O6 perovskites: a review," vol. 43, no. 1-2, pp. 1-36, 2015.

[89]   A. Maignan, C. Martin, D. Pelloquin, N. Nguyen, and B. J. J. o. S. S. C. Raveau, "Structural and magnetic studies of ordered oxygen-deficient PerovskitesLnBaCo2O5+ δ, closely related to the "112" structure," vol. 142, no. 2, pp. 247-260, 1999.

[90]   S. Sengodan $et\ al.$, "Layered oxygen-deficient double perovskite as an efficient and stable anode for direct hydrocarbon solid oxide fuel cells," vol. 14, no. 2, pp. 205-209, 2015.

[91]   S. Geiger $et\ al.$, "The stability number as a metric for electrocatalyst stability benchmarking," vol. 1, no. 7, pp. 508-515, 2018.

[92]   A. Grimaud $et\ al.$, "Double perovskites as a family of highly active catalysts for oxygen evolution in alkaline solution," vol. 4, no. 1, pp. 1-7, 2013.

[93]   L. Zhou, Y. F. Xu, B. X. Chen, D. B. Kuang, and C. Y. J. S. Su, "Synthesis and Photocatalytic Application of Stable Lead-Free Cs2AgBiBr6 Perovskite Nanocrystals," vol. 14, no. 11, p. 1703762, 2018.

[94]   R. A. Rincón, J. Masa, S. Mehrpour, F. Tietz, and W. J. C. c. Schuhmann, "Activation of oxygen evolving perovskites for oxygen reduction by functionalization with Fe–N x/C groups," vol. 50, no. 94, pp. 14760-14762, 2014.

[95]   K. Elumeeva $et\ al.$, "A Simple Approach towards High-Performance Perovskite-Based Bifunctional Oxygen Electrocatalysts," vol. 3, no. 1, pp. 138-143, 2016.

[96]   K. Elumeeva, J. Masa, J. Sierau, F. Tietz, M. Muhler, and W. J. E. a. Schuhmann, "Perovskite-based bifunctional electrocatalysts for oxygen evolution and oxygen reduction in alkaline electrolytes," vol. 208, pp. 25-32, 2016.

[97]   J.-I. Jung *et al.*, "Optimizing nanoparticle perovskite for bifunctional oxygen electrocatalysis," vol. 9, no. 1, pp. 176-183, 2016.

[98]   J. I. Jung, H. Y. Jeong, J. S. Lee, M. G. Kim, and J. J. A. C. Cho, "A bifunctional perovskite catalyst for oxygen reduction and evolution," vol. 126, no. 18, pp. 4670-4674, 2014.

[99]   G. Liu *et al.*, "Hierarchical mesoporous/macroporous perovskite La0. 5Sr0. 5CoO3–x nanotubes: a bifunctional catalyst with enhanced activity and cycle stability for rechargeable lithium oxygen batteries," vol. 7, no. 40, pp. 22478-22486, 2015.

[100]   D. U. Lee *et al.*, "Highly active Co-doped LaMnO3 perovskite oxide and N-doped carbon nanotube hybrid bi-functional catalyst for rechargeable zinc–air batteries," vol. 60, pp. 38-41, 2015.

[101]   D. Zhang, Y. Song, Z. Du, L. Wang, Y. Li, and J. B. J. J. o. M. C. A. Goodenough, "Active LaNi 1− x Fe x O 3 bifunctional catalysts for air cathodes in alkaline media," vol. 3, no. 18, pp. 9421-9426, 2015.

[102]   M. Prabu, P. Ramakrishnan, P. Ganesan, A. Manthiram, and S. J. N. E. Shanmugam, "LaTi0. 65Fe0. 35O3− δ nanoparticle-decorated nitrogen-doped carbon nanorods as an advanced hierarchical air electrode for rechargeable metal-air batteries," vol. 15, pp. 92-103, 2015.

[103]   H. W. Park, D. U. Lee, P. Zamani, M. H. Seo, L. F. Nazar, and Z. J. N. E. Chen, "Electrospun porous nanorod perovskite oxide/nitrogen-doped graphene composite as a bi-functional catalyst for metal air batteries," vol. 10, pp. 192-200, 2014.

[104]   Y. Zhu, W. Zhou, J. Yu, Y. Chen, M. Liu, and Z. J. C. o. M. Shao, "Enhancing electrocatalytic activity of perovskite oxides by tuning cation deficiency for oxygen reduction and evolution reactions," vol. 28, no. 6, pp. 1691-1697, 2016.

[105]   Y. Zhao *et al.*, "Hierarchical mesoporous perovskite La0. 5Sr0. 5CoO2. 91 nanowires with ultrahigh capacity for Li-air batteries," vol. 109, no. 48, pp. 19569-19574, 2012.

[106]   M. Y. Oh, J. S. Jeon, J. J. Lee, P. Kim, and K. S. J. R. A. Nahm, "The bifunctional electrocatalytic activity of perovskite La 0.6 Sr 0.4 CoO 3− δ for oxygen reduction and evolution reactions," vol. 5, no. 25, pp. 19190-19198, 2015.

[107] J. Park, M. Park, G. Nam, M. G. Kim, and J. J. N. l. Cho, "Unveiling the catalytic origin of nanocrystalline yttrium ruthenate pyrochlore as a bifunctional electrocatalyst for Zn–Air batteries," vol. 17, no. 6, pp. 3974-3981, 2017.

[108] Z. Du et al., "Electrocatalytic performances of LaNi1− xMgxO3 perovskite oxides as bi-functional catalysts for lithium air batteries," vol. 265, pp. 91-96, 2014.

[109] Z. Wang et al., "Nickel-Doped La0. 8Sr0. 2Mn1–x Ni x O3 Nanoparticles Containing Abundant Oxygen Vacancies as an Optimized Bifunctional Catalyst for Oxygen Cathode in Rechargeable Lithium–Air Batteries," vol. 8, no. 10, pp. 6520-6528, 2016.

[110] D. Wang, X. Chen, D. G. Evans, and W. J. N. Yang, "Well-dispersed Co 3 O 4/Co 2 MnO 4 nanocomposites as a synergistic bifunctional catalyst for oxygen reduction and oxygen evolution reactions," vol. 5, no. 12, pp. 5312-5315, 2013.

[111] Y. Gorlin and T. F. J. J. o. t. A. C. S. Jaramillo, "A bifunctional nonprecious metal catalyst for oxygen reduction and water oxidation," vol. 132, no. 39, pp. 13612-13614, 2010.

[112] J. Hu, Q. Liu, Z. Shi, L. Zhang, and H. J. R. a. Huang, "LaNiO 3-nanorod/graphene composite as an efficient bi-functional catalyst for zinc–air batteries," vol. 6, no. 89, pp. 86386-86394, 2016.

[113] B. Hua et al., "Stabilizing double perovskite for effective bifunctional oxygen electrocatalysis in alkaline conditions," vol. 29, no. 15, pp. 6228-6237, 2017.

[114] F. Lu, Y. Wang, C. Jin, F. Li, R. Yang, and F. J. J. o. P. S. Chen, "Microporous La0. 8Sr0. 2MnO3 perovskite nanorods as efficient electrocatalysts for lithium–air battery," vol. 293, pp. 726-733, 2015.

[115] W. Li et al., "Evaluation of double perovskite Sr2FeTiO6− δ as potential cathode or anode materials for intermediate-temperature solid oxide fuel cells," vol. 41, no. 9, pp. 12393-12400, 2015.

[116] J. Xu, X. Zhou, X. Dong, L. Pan, and K. J. I. J. o. H. E. Sun, "Catalytic activity of infiltrated La0. 3Sr0. 7Ti0. 3Fe0. 7O3− δ–CeO2 as a composite SOFC anode material for H2 and CO oxidation," vol. 42, no. 23, pp. 15632-15640, 2017.

[117] H. R. Nodeh and H. J. R. a. Sereshti, "Synthesis of magnetic graphene oxide doped with strontium titanium trioxide nanoparticles as a nanocomposite for

the removal of antibiotics from aqueous media," vol. 6, no. 92, pp. 89953-89965, 2016.

[118] M. O. Amuanyena, M. Kandawa-Schulz, H. M. J. J. o. B. Kwaambwa, and Nanobiotechnology, "Magnetic Iron Oxide Nanoparticles Modified with Moringa Seed Proteins for Recovery of Precious Metal Ions," vol. 10, no. 02, p. 142, 2019.

[119] J. Wang *et al.*, "Ba0. 5Sr0. 5Co0. 8Fe0. 2O3− δ on N-doped mesoporous carbon derived from organic waste as a bi-functional oxygen catalyst," vol. 41, no. 25, pp. 10744-10754, 2016.

[120] Q. A. Islam, R. Majee, and S. J. J. o. M. C. A. Bhattacharyya, "Bimetallic nanoparticle decorated perovskite oxide for state-of-the-art trifunctional electrocatalysis," vol. 7, no. 33, pp. 19453-19464, 2019.

[121] P. Wang *et al.*, "Three-dimensional heterostructured NiCoP@ NiMn-layered double hydroxide arrays supported on Ni foam as a bifunctional electrocatalyst for overall water splitting," vol. 12, no. 4, pp. 4385-4395, 2019.

[122] J. Liu *et al.*, "Hierarchical NiCo2S4@ NiFe LDH heterostructures supported on nickel foam for enhanced overall-water-splitting activity," vol. 9, no. 18, pp. 15364-15372, 2017.

[123] Y. Gogotsi and R. M. Penner, "Energy storage in nanomaterials–capacitive, pseudocapacitive, or battery-like?," ed: ACS Publications, 2018.

[124] N. Shuhaimi, L. Teo, H. Woo, S. R. Majid, and A. K. J. P. b. Arof, "Electrical double-layer capacitors with plasticized polymer electrolyte based on methyl cellulose," vol. 69, no. 7, pp. 807-826, 2012.

[125] Y.-P. Gao, K.-J. Huang, X. Wu, Z.-Q. Hou, Y.-Y. J. J. o. a. Liu, and compounds, "MoS2 nanosheets assembling three-dimensional nanospheres for enhanced-performance supercapacitor," vol. 741, pp. 174-181, 2018.